Non-Destructive Determination of Chloride and Water Content in Concrete Using Ground Penetrating Radar

PAR

Alexis KALOGEROPOULOS

EPFL

ÉCOLE POLYTECHNIQUE
FÉDÉRALE DE LAUSANNE

Suisse
2012

Ἐπεὶ δ’ ἡ φύσις μέν ἐστιν ἀρχὴ κινήσεως καὶ μεταβολῆς, ἡ δὲ μέθοδος ἡμῖν περὶ φύσεώς ἐστι, δεῖ μὴ λανθάνειν τί ἐστι κίνησις. ἀναγκαῖον γὰρ ἀγνοουμένης αὐτῆς ἀγνοεῖσθαι καὶ τὴν φύσιν.

"Nature has been defined as a principle of motion and change, and it is the subject of our inquiry. We must therefore see that we understand the meaning of motion; for if it were unknown, the meaning of nature too would be unknown."

Aristotle, Physics, Book III,1. 350 BC.

Aux miens,
aux précédents et aux suivants …

Acknowledgements

The Ph.D. was done under the supervision of Dr. Johannes Hugenschmidt, Prof. Jan van der Kruk and Prof. Eugen Brühwiler. The author would like to thank them, for their listening, advices and patience; this adventure was wonderful at your sides.

The author would also like to thank, Dr. Roman Loser and Dr. Xavier Dérobert, for their active contribution to this work.

Finally, the author would like to thank the staff from EMPA, EPFL, ETHZ, and Forschungszentrum-Jülich. Their help and dedication allowed this work to be done in the best conditions.

Lausanne, 24 April 2012   A. K.

Abstract

Abstract Corrosion of rebar within reinforced concrete is a major problem for countries where salt is applied to roads for deicing. Concrete structures are periodically inspected in order to monitor possible damage caused by chloride-induced corrosion of the reinforcement. However, the available drilling and visual inspections do not supply sufficient spatial information or can only be assessed in advanced stages of corrosion, respectively. Consequently, the condition of bridge decks can only be assessed with low certainty. Therefore, a spatially continuous and non-destructive method detecting chloride in concrete structures is desirable. This Ph.D. thesis deals with the non-destructive monitoring of chloride ion concentration inside the concrete of bridge decks, in the case of seasonal exposition to chlorides. Novel Ground Penetrating Radar data processing methodologies and their prerequisites are presented. An experiment recreating chloride contamination processes in concrete was designed. From it, a Ground Penetrating Radar dataset was acquired. The dataset was processed with these novel methodologies. The results analysis enabled the constitution of empiric relationships linking concrete condition and Ground Penetrating Radar datasets.

Résumé La corrosion des barres d'armature des structures en béton armé est un probème majeur, dans les pays où le sel est appliqué sur les routes pour le dégivrage. Les structures en béton armé sont inspectés périodiquement afin de suivre les éventuels dommages de corrosion induits par des ions chlorures apportés par les sels de dégivrage. Cependant, les inspections visuelles ainsi que les campagnes de carottage ne fournissent pas suffisamment d'information spatiale ou ne peuvent évaluer qu'un stade de corrosion avancé. Par conséquent, le relevé de l'état des tabliers de pont ne peut être que difficilement évalué. Une méthode non-destructive de détection de chlorure dans les structures en béton est ainsi souhaitable. Cette thèse traite du monitoring non-destructif de la concentration en ions chlorure dans le béton des tabliers de pont, dans le cas d'expositions saisonnières aux chlorures, á l'aide d'un Géoradar. De nouvelles méthodologies de traitement de données Géoradar et de leurs conditions préalables sont présentées. Une expérience recréant les processus de contamination de chlorure dans le béton a été conçue. De là, un ensemble de données Géoradar ont été acquises. L'ensemble des données ont été traitées avec les nouvelles méthodologies développées dans cette thèse. L'analyse des résultats a permis la constitution de relations empiriques reliant la contamination par chlorures du béton avec les données Géoradar.

Acknowledgements

Contents

Contents

Introduction

This Ph.D. thesis presents methodologies for the non-destructive determination of chloride content in concrete. They are developed having for objective to monitor chloride contamination level within the concrete of bridge decks, using Ground Penetrating Radar.

Chloride induced reinforced concrete corrosion

Chloride contamination   During winter, salt is applied on roads for deicing. When salt crystals reach water mixed with snow and ice, they start to dissolve into chloride Cl- and sodium ions Na+. Their presence in the water lowers the freezing temperature and prevents the melted mixture to freeze again. In this way, bonding between the ice layer and the bridge surface is prevented.The chloride ions dissolved in melt water will progressively pass through the pores and cracks of the asphalt layer. Consequently, saline water will accumulate at the interface between asphalt and concrete. Thereafter, the solution gradually migrates through the concrete pores reaching the reinforcement layer. During drying, water evaporates without mobilizing chlorides that remain inside the concrete. In this way, the seasonal variation causes the chlorides to gradually migrate through the pores of the concrete by capillarity and diffusion processes, see Conciatori, 2005, [6]. As a consequence of these transportation processes it is expected for chloride ions, to be distributed in gradients within a concrete structure, see Appendix III.

Corrosion   Reinforced concrete structures and specifically bridge decks contain several layers of steel reinforcement bars (rebars) for structural resistance. Once chlorides reach the first rebar layer, generally, located at 2-4 cm depth. The chloride ions remove the protecting passivation layer on the steel rebar surface and localized corrosion, pitting, initiates. Different studies have shown that the probability corrosion initiation increases steadily with increasing chloride levels. This probability is considered high when chloride content exceeds 0.5% of cement mass on top of the reinforcement, see Böhni, 2005, [3]. Once initiated, the corrosion process does not stop and the rebars progressively lose their mechanical resistance until possible structural failure.

1

Non-destructive assessment of reinforced concrete structures using GPR

Ground penetrating radar   Ground penetrating radar (GPR) is a non-destructive technique based on the emission and reception of electromagnetic (EM) waves. GPR has the advantage, in the case of bridge decks inspection, to map the structure without the need to strip the asphalt layer nor interrupting the traffic. The use of GPR technology is commonly described in literature for reinforced concrete structural mapping, [16, 8, 19, 2, 36]. Several authors studied the effect of water and chloride effect on GPR datasets,[27, 26, 34, 13, 40, 23, 22, 29, 12, 32, 37, 24]. Finally, other non-destructive testing techniques for corrosion and free chloride detection were developed and presented in literature,[9, 10, 4, 5, 1, 31]. Even they provide accurate results, these non-destructive methods are generally less advantageous than GPR when comparing data acquisition speed. However a GPR data processing enabling the combined estimation of the electromagnetic parameters and the relation liking them with water and chloride content are missing.

The electromagnetic parameters ε_r and σ   Maxwell's equations explains how an electromagnetic wave propagates in a non-magnetic dielectric medium. The velocity and the damping experienced by the wave will vary with the conductivity (σ) and the relative dielectric permittivity (ε_r) of the medium. GPR generates pulses in a domain ranging from 1.10^6 to 5.10^9 Hz. Within this bandwidth, Laws of electromagnetism define σ as the capacity of a dielectric to conduct electrical currents. These currents, expressed in Siemens per m [S/m], are produced by the displacement of charged free particles inside the dielectric, for instance, dissolved Cl- ions within the solution present inside the concrete pores. The relative dielectric permittivity ε_r is the ratio between dipolar rotational velocity of the molecules constituting a dielectric and void. ε_r influences the wave propagation velocity and because it is a ratio, it is unit-less [-]. Each dielectric material has its own ε_r and σ, for instance, air and a concrete slab contaminated with saline water. Finally at each boundary, between two dielectrics, the pulse will separate into a reflected and a transmitted wave. The angle of transmission and reflection plus the proportion between the transmitted and reflected energy are given by Snell's-Descartes Law and Fresnel's coefficients, respectively, see Appendix I.

Interest of research

Several studies have shown the influence of chloride and moisture on GPR datasets, Robert, 1998, [32]; Hugenschmidt and Loser, 2006, [15]. Recently, Full-waveform GPR data inversion methodologies brought the possibility to quantify ε_r and σ of the investigated objects: Crocco and Soldovieri 2003, [7]; Lambot *et al.*, 2004, [28]; van der Kruk *et al.*, 2006 [39]; Ernst *et al.*, 2007, [11]; Jadoon *et al.*, 2008, [17]; Meles *et al.*, 2010, [30]; Klotzsche *et al.*, 2010, [20]. With the expression of chloride and moisture content effect on both ε_r and σ, the combination of the structure's mapping with the EM parameters will account for the bridge deck condition and it's chloride contamination level.

This document has for objective, to describe two methodologies and their prerequisite for the calculation relative dielectric permittivity and the conductivity from GPR data. There-after, using experimental GPR datasets the relation between the electromagnetic parameters with chloride and water content is showed. This document is composed of three paper-like chapters:

* *Chloride and moisture assessment in concrete by full-waveform inversion*, was written with the contribution of Jan van der Kruk, Johannes Hugenschmidt, Sebastian Bush and Kaspar Merz. It was published in 2011, in Near Surface Geophysics, Journal. This paper describes the prerequisites to Full-waveform inversion. Calculates averages values of the electromagnetic parameters returned from a GPR experimental dataset presented by Hugenschmidt and Loser, 2006, [15]. Then the influence of chloride and moisture content on the electromagnetic parameters is discussed.

* *Determining the electromagnetic parameters of concrete with chloride gradients using GPR,* was written with the contribution of Jan van der Kruk, Johannes Hugenschmidt, Jutta Bikowski and Eugen Brühwiler. The Full-waveform inversion methodology is up-dated and enables the determination of gradients of conductivities within a concrete slab. In parallel, a light computational Time Domain Solution was developed; it provides average values of the concrete slab electromagnetic parameters. The results, to-gether with additional destructive testing, allowed relation of the chloride gradient dis-tribution influence on the concrete specimen electromagnetic parameters.

* *Monitoring of chloride ion concentration in concrete using GPR,* was written with the contribution of Jan van der Kruk, Johannes Hugenschmidt, Roman Loser and Eugen Brühwiler. An experimental GPR dataset on concrete specimens, experiencing cyclic chloride contamination, is processed with Time Domain Solution. The results enabled to build empiric relationships between chloride and water content with the electro-magnetic parameters.

The document is completed with four appendixes. Appendix I, presents the Laws of elec-tromagnetism and their implications in GPR. Appendix II, presents the assessment of the simplifications used with Time Domain Solution. Appendix III, explains the chloride con-tamination processes within concrete. And finally Appendix IV, presents a real case study where maps of concrete cover, moisture content and an estimation of chloride content, are provided. The results are in accordance with targeted probing taken on the bridge.

1 Chloride and moisture assessment in concrete by full-waveform inversion

Abstract   Corrosion of rebar within reinforced concrete is a major problem for countries where salt is applied to roads for deicing. Concrete structures are periodically inspected in order to monitor possible damage caused by chloride-induced corrosion of the reinforcement. However, the available drilling and visual inspections do not supply sufficient spatial information or can only be assessed in advanced stages of corrosion, respectively. Consequently, the condition of bridge decks can only be assessed with low certainty. Therefore, a spatially continuous and non-destructive method detecting chloride in concrete structures is desirable. This paper describes a novel method to estimate material properties using the Full-waveform inversion of bi-static off-ground ground penetrating radar data. In this way, all information present in the ground-penetrating radar (GPR) traces is used, which enables the estimation of quantitative electromagnetic properties. A critical step for Full-waveform inversion is a proper characterization of the horn antenna GPR system by estimating the phase centre and the effective wavelet using measurements over a stainless steel plate. The inversion of GPR data measured over nine concrete specimens having different moisture and chloride contents returned a relative dielectric permittivity and a conductivity that included a frequency-dependent component. As expected, the inversion results for almost all specimens showed for increasing chloride and humidity content specimens increasing conductivity and permittivity values, respectively. For increasing chloride content, increasing frequency-dependent conductivity values were obtained.

Johannes Hugenschmidt, EMPA, Switzerland
Jan Van Der Kruk, Forschungszentrum Jülich, Germany
Sebastian Busch, Forschungszentrum Jülich, Germany
Kaspar Merz, ETH Zurich, Switzerland

Alexis Kalogeropoulos, EMPA, Switzerland;
Corresponding Author: j.van.der.kruk@fz-juelich.de

1.1 Introduction

Nowadays, the assessment of existing concrete structures is a major challenge for civil engineers and an important issue is reinforcement corrosion. Structures like bridges are exposed to corrosion because of salt spread in winter for road deicing. Ground penetrating radar (GPR) presents several abilities for their assessments: GPR I) is non destructive, II) can locate changes of medium conditions and III) allows keeping the structure open for traffic during its inspection. Therefore, GPR is a suitable non-destructive tool to investigate reinforced concrete bride decks, Sbartai *et al.* 2006, [35]; Hugenschmidt and Mastrangelo 2006, [16]; Klysz and Balayssac 2007, [21]; Dérobert *et al.* 2008, [8]. Previous experimental assessment carried out with GPR measurements over nine concrete specimens with controlled chloride and moisture content, Hugenschmidt and Loser 2007[15], demonstrated that amplitudes of reflections are influenced by both the chloride and moisture content. However, it was not possible to discriminate between moisture and chloride effects. Recently, several Full-waveform inversions have been developed that enable quantitative estimation of medium properties by fitting the whole measured waveform with an accurate forward model, Crocco and Soldovieri 2003, [7]; Lambot *et al.* 2004, [28]; Ernst *et al.* 2007, [11]; Meles *et al.* 2010, [30]; Klotzsche *et al.* 2010, [20]). This paper describes the processing of experimental GPR data and analyses the influence of chlorides and moisture on estimations of conductivity and relative dielectric permittivity provided with a Full-waveform inversion. Finally, discusses the stability of these results.

1.2 Basics of steel corrosion due to the presence of chlorides

During winter, salt is used for road deicing. The chlorides dissolved in the melt water are scattered around the reinforced concrete structure mainly due to vehicle circulation. Once the impermeability of the sealing is compromised, the water containing chlorides penetrates into the underlying concrete during wet seasons. During dry seasons water evaporates without mobilizing chlorides that remain in the concrete. The alternation of weathering cycles causes the chlorides to gradually migrate through the pores of the concrete by capillarity and diffusion, Conciatori 2005, [6]. Thus, one can expect to encounter chloride and water concentration gradients within a concrete structure. Reinforced concrete structures and specifically bridge decks contain several layers of steel reinforcing bars (rebars) for bearing resistance. Once chlorides reach the first rebar layer, generally located at 2-4 cm depth, the chloride ions remove the protecting passivation layer on the steel rebar surface and localized corrosion pitting, is initiated. Pitting corrosion induces localized areas to become anodic, while the rest of the bar becomes cathodic. This creates an electric potential that increases the corrosion process. Different studies have shown that the probability of the initiation increases steadily with increasing chloride levels. This probability is considered high when exceeding 0.5% chloride content, Böhni 2005, [3]. Once initiated, the corrosion process does not stop and the rebars lose progressively their mechanical resistance until possible structural failure.

	Moisture		
Chloride	35%	70%	90%
1%	7	8	9
0.4%	4	5	6
0%	1	2	3

Table 1.1: Specimen numeration.

1.3 Experimental setup

In order to evaluate the effect of chlorides and moisture on ground penetrating radar signals, experiments were carried out by measuring traces with fixed-height horn antennas over concrete slabs having controlled moisture and chloride content.

Concrete specimens Nine concrete slabs were produced in Hugenschmidt and Loser 2007, [15] experiment, each with dimensions of 0.90 [m], 0.75 [m] and 0.08 [m]. Three concrete mixtures with a constant volume of paste but different chloride contents were used, see Table 1.1. Chlorides were added to the mixtures by dissolving NaCl in the mixing water. All mixtures had comparable fresh concrete properties. The concrete was cast in three moulds per mixture and the bases of the moulds were covered with aluminum sheets. After compaction, the specimens were stored at 20 degrees Celsius and 90% relative humidity for two days. Afterwards, one specimen of each mixture was moved to climates of 35%, 70% and 90% relative humidity for 99 days before the radar measurements were carried out. One would expect to obtain higher increasing relative dielectric permittivity ε_r for increasing water content and higher increasing conductivity σ for increasing chloride content.

GPR measurements The measurements were performed using two off-ground 1.2 [GHz] horn antennas with an offset of 0.28 [m] and positioned at a fixed height, h = 0.25 [m], above the concrete specimens, see Fig. 1.1. A representative trace is shown in Fig. 1.2. For calibration purposes, also measurements were performed over stainless-steel plates for different heights, see Fig. 1.4.

1.4 Forward model

To perform a Full-waveform inversion of GPR data, an accurate forward model is necessary that describes the medium properties and the electromagnetic wave propagation from source to concrete specimen and back to the receiver.

Medium properties The analysis of the normalized frequency spectrum of the concrete-aluminum interface reflection from recorded data revealed that for increasing chloride contents, the high frequencies had lower amplitudes, Fig. 1.6. These relatively lower amplitudes for higher frequencies indicate a frequency dependent conductivity assessed by several authors, Robert 1998, [32]; Soutsos *et al.* 2001, [37]; Lambot *et al.* 2004, [28]. To include the
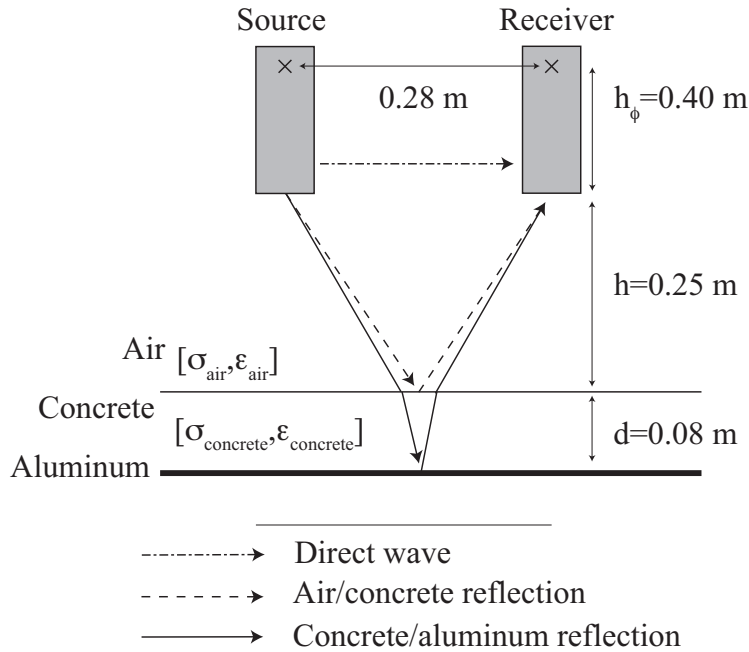
Figure 1.1: Measurement setup of off-ground horn antennas with an offset between the source and receiver antenna of 0.28 m. Ray-paths indicate the simplified travel-paths of direct wave, air/concrete and concrete/aluminum reflections.
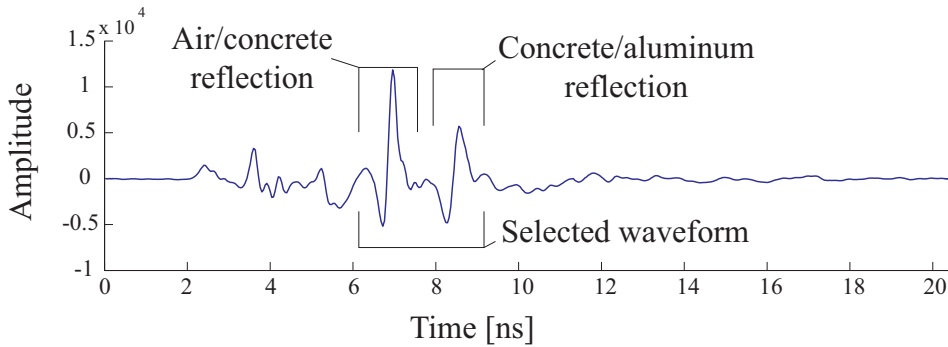
Figure 1.2: Trace recorded on the concrete specimen showing two reflections coming from air/concrete and concrete/aluminum interfaces. Corresponding simplified travel-paths are shown in Fig.1.1

8
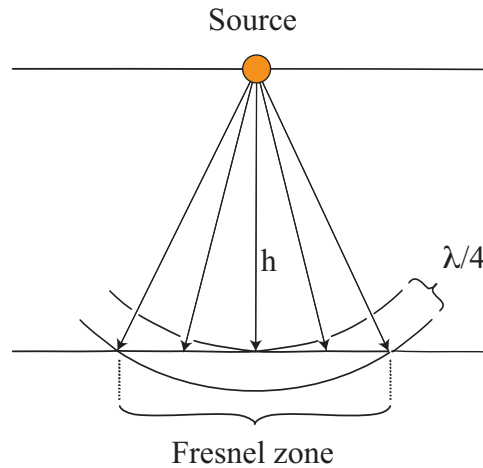
Figure 1.3: Fresnel zone calculations are used to consider only the reflected energy coming from the stainless-steel plate during phase centre estimation.

frequency-dependent conductivity in the model, the following equation was used:

$$\sigma(f, \sigma_{f_c}, \Delta\sigma) = \sigma_{f_c} + \frac{f - f_c}{f_c}\Delta\sigma. \tag{1.1}$$

Where f_c is the centre frequency of the GPR system 1.2 [GHz], σ_{f_c} is the reference electric conductivity at the centre frequency and $\Delta\sigma$ is the frequency dependent part of $\sigma(f, \sigma_{f_c}, \Delta\sigma)$. The frequency dependence of the relative permittivity was assumed to be negligible, see Lambot et al. 2004, [28].

Green's function   The antennas were modeled as point sources that emit an effective wavelet $\hat{W}$. In the frequency domain, the electric field can be written as:

$$\hat{E}_{model}(f) = \hat{G}(f, \varepsilon_r, \sigma)\hat{W}(f). \tag{1.2}$$

Where $\hat{G}$ is the Green's function that describes the wave propagation for a horizontally layered medium, see also van der Kruk et al. 2006, [39]. Since the wavelet is unknown, we need the calibration setup shown in Fig. 1.4 and introduce the following Green's function:

$$\hat{G}(f, \varepsilon_r, \sigma) = \hat{G}^{as}(f, \varepsilon_r, \sigma), \tag{1.3}$$

where $\hat{G}^{as}$ describes the total reflection of a wave propagating from the source to a stainless steel plate and its back-propagation to the receiver, Fig. 1.4. For the concrete measurements, two reflections are measured, see Fig 1.2. The corresponding Green's function includes the source-reflector and reflector-receiver propagation plus both reflections coming from the concrete specimen interfaces, which can be written like so:

$$\hat{G}(f, \varepsilon_r, \sigma) = \hat{G}^{ac}(f, \varepsilon_r, \sigma) + \hat{G}^{ca}(f, \varepsilon_r, \sigma), \tag{1.4}$$

where $\hat{G}^{ac}$ and $\hat{G}^{ca}$ stand for the propagation of the first reflection on the air/concrete interface and the second reflection of the concrete/aluminum interface, respectively.

1.5 GPR system characterization

A critical step for Full-waveform inversion is a proper characterization of the GPR system, Klotzsche *et al.* 2010, [20]. The forward model describes measurements assuming a point source and receiver. In reality, these antennas are horn antennas,where the waves are guided within them and spread spherically while outside. The calibration procedure described by Lambot *et al.* 2004, [28], where a monostatic off-ground antenna system was used in combination with a Vector Network Analyzer. Here this is not possible since the measurements were carried out using a commercial GPR system. The GPR system was described estimating a phase centre and an effective wavelet when the system was measuring reflections coming from a stainless-steel plate.
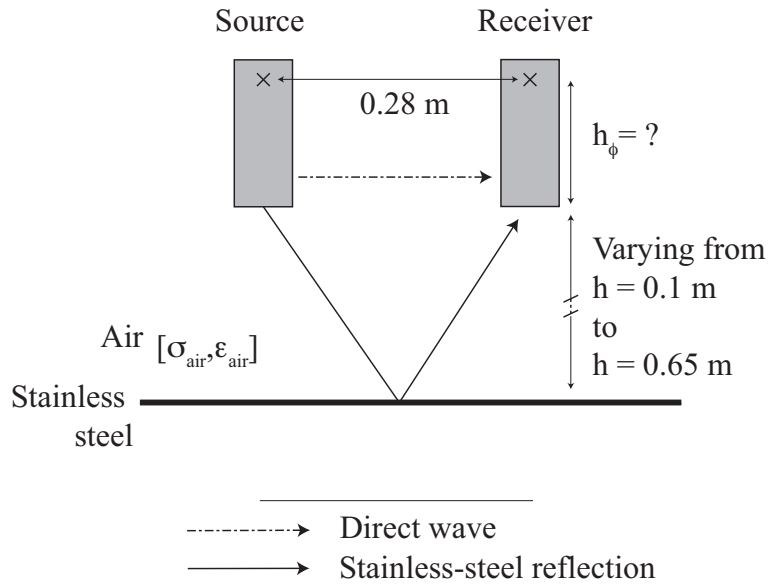
Figure 1.4: Antenna calibration setup over a stainless-steel plate.
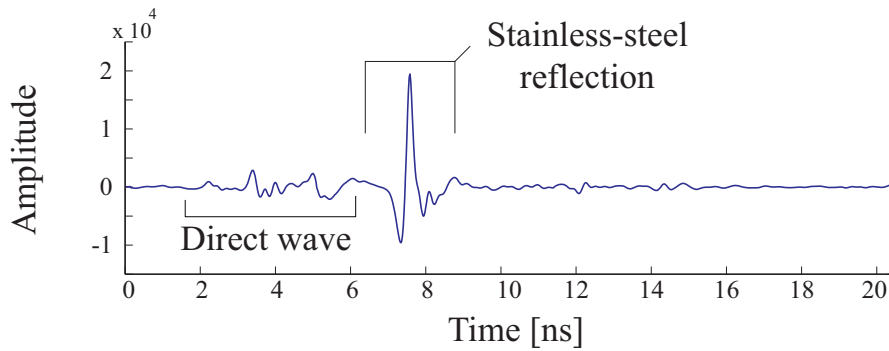
Figure 1.5: Calibration trace recorded for time-zero positioning and effective wavelet estimation. The direct wave is present between 2 to 6 [ns]. The high-amplitude reflection from stainless-steel interface is present around 8 [ns].
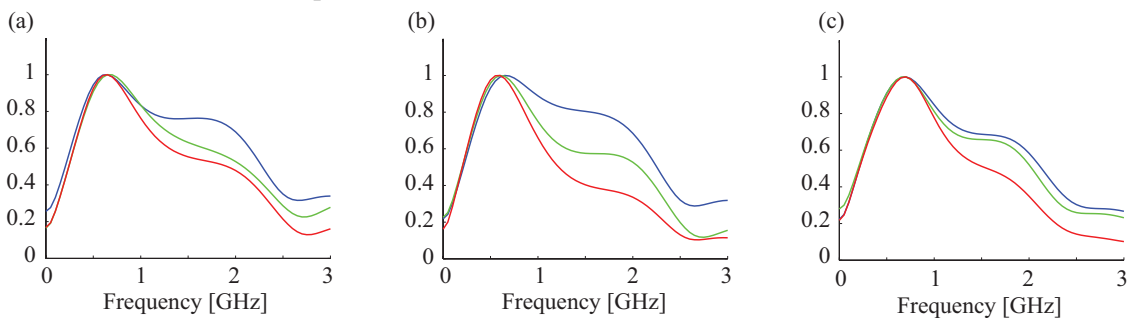
Figure 1.6: Normalized frequency spectrums of measured traces for a) 35%, b) 70% and c) 90% relative humidity and 0% (blue), 0.4% (green) and 1% (red) chloride content. For increasing conductivity, the high-frequency amplitudes are reduced more than the low frequencies. This indicates a frequency dependent conductivity at high-frequencies.

Phase centre estimation The phase centre is the virtual point from which the electromagnetic waves seem to be emitted or received assuming point source and receiver antennas, see Fig. 1.4. To estimate the phase centre, a calibration was performed by measuring the reflections coming from a stainless-steel plate for heights varying between 0.1 < h < 0.65 [m], Fig. 1.4. A time-domain filter was used to select the stainless-steel reflection, see Fig. 1.5. Additionally, we used the Fresnel zone to ascertain that only the reflections from the specimen will be inverted and no side reflections influence the results. The Fresnel Zone (Fig. 1.3) is the diameter of a circle from which the reflections constructively interfere. The travel-path between the vertical incident ray and the ray from the boundary of the Fresnel zone has a half-wavelength difference in the travel-path, it is given by:

$$\text{Fresnel zone} = \sqrt{\frac{0.6.h}{f}}, \tag{1.5}$$

where h is height in [m] and f is frequency given in [GHz]. The Fresnel zone can be used to estimate the lowest frequency from which all reflections come from the surface of the stainless-steel plate and not from its sides. Taking the smallest horizontal dimension of the concrete specimen, 0.75 [m] and a maximum height of h = 0.65 [m] to calculate the lowest frequency from which the side effects have no influence on the measurements, we get 700 [MHz] as a lower limit. Note that the phase centre is not included in the Fresnel zone calculation since the waves are guided within the antenna. The amplitudes from the surface reflection of the stainless steel plate decrease with 1/(travel distance) or 1/(2 height) due to the geometrical spreading when measured in the far-field. By plotting the inverse values of representative amplitudes within the wavelet as a function of the travel distance, or height, we can extrapolate towards zero amplitude using a linear regression approach that indicates the position of the phase centre, Lambot *et al.* 2004, [28]. Here, we used the maximum, minimum-maximum and energy values of the reflected waveforms, which returned a similar value of the phase centre, $h_\phi = 0.40$ [m], see Fig. 1.7.

Effective wavelet estimation The effective wavelet is determined to describe the wavelet that is emitted and received by the antennas. It is extracted for each specimen by spectral division of a calibration measurement and a Green's function, see Streich and van der Kruk 2007, [38]; Ernst *et al.* 2007 [11]; Klotzsche *et al.* 2010, [20]:

$$\hat{W}(f) = \frac{\hat{E}_{ref}(f)\hat{G}^{as*}(f)}{\hat{G}^{as}(f)\hat{G}^{as*}(f) + 10^{-10}}, \tag{1.6}$$

where $\hat{E}_{ref}$ is the calibration trace with corresponding height, $h + h_\phi = 0.65$ [m], used for the inversion measurements, see also Fig. 1.5. $\hat{G}_{as}$ is the calculated Greens function, in equation 1.3, describing a total reflection of the incident wave on the stainless-steel plate surface assuming a reflection coefficient of -1. The value 10^{-10} is used to avoid division by zero. Figure 1.8, shows the estimated wavelet and three frequency-filtered wavelets used in the inversion.

1.6 Full-waveform inversion methodology

The dataset, measured with a 1.2 [GHz] antenna centre frequency, contains frequencies between 500 [MHz] and 2.1 [GHz]. It was inverted using three different frequency ranges: 0.575-
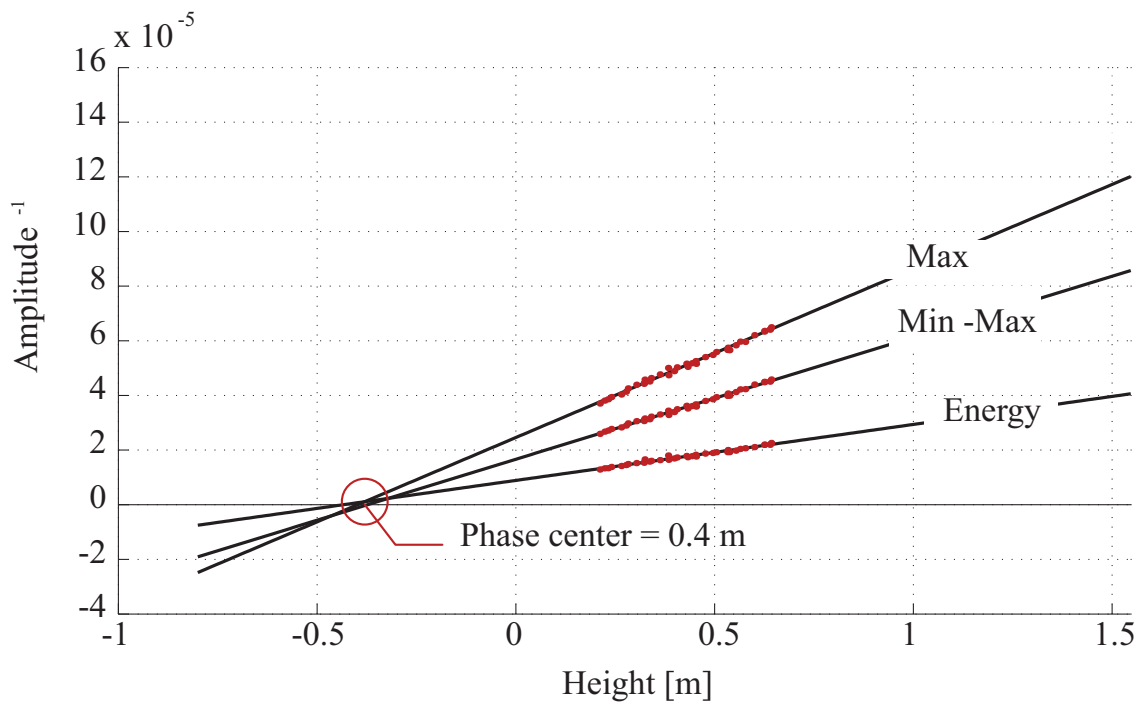
Figure 1.7: Linear regression using the inverse values of reflected calibration waveform values (maximum, minimum-maximum and energy) to estimate the phase centre.
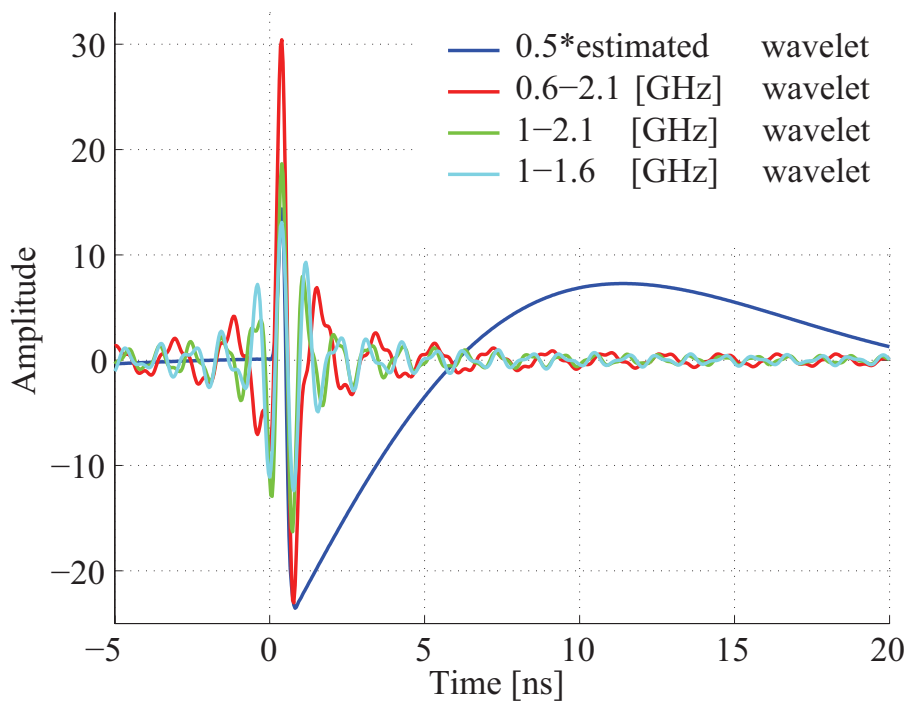

Figure 1.8: Estimated wavelet, halved in amplitude, with three frequency-filtered wavelets used in the inversion.

2.1 [GHz], 1-2.1 [GHz] and 1-1.625 [GHz] using the corresponding wavelet shown in Fig. 1.8. After estimating the phase centre and the effective wavelet, synthetic GPR data with configuration parameters according to the measurements are modeled using equations 1.1, 1.2 and 1.4. In the following, model parameters **m** describe the wave propagation within the concrete slab that are optimized for n frequencies by minimizing the misfit between the measurement and synthetic data:

$$C(\mathbf{m}) = \sum_{i=1}^{n} \frac{|\hat{E}_{Data} - \hat{G}(f_i, \mathbf{m})\hat{W}(f_i)|}{n}. \tag{1.7}$$

Start model   For Full-waveform inversion the start model is important. Using a start model that is far away from the actual global minimum can result in a wrong result due to the presence of local minima. To improve the robustness of our inversion strategy against local minima and to assure convergence towards the global minimum returning the true values of the electric features of the concrete slabs, we used the picked time-zero and the maximum and minimum of both air/concrete and concrete/aluminum reflections as start values in the inversion algorithm. Moreover, we used several start models in the three consecutive steps of the inversion algorithm to investigate the convergence. For each start model, a local optimization algorithm based on the simplex search algorithm, Lagarias et al. 1998, [25], was initiated and a local minimum was found. The local minimum with the smallest cost function is assumed to be the global minimum.

Inversion first step   The first step optimized the time-zero and the concrete permittivity ($\mathbf{m1} = [t_0, \varepsilon_r]$) by minimizing the misfit between the measured air/concrete reflection with $\hat{G}^{ac}\hat{W}$, see equations 1.4 and 1.7. A correction for the time-zero is needed since a stainless-steel plate was put on the specimen for the calibration measurements, which slightly changes the vertical location of the reflection. In this step, the frequency-dependent conductivity was not optimized since the air/concrete reflection mainly depends on the concrete permittivity. Two starting values for time-zero are obtained by taking the picked time-zero, ± 1 sample. Two starting values for permittivity are derived, by picking the maximum and minimum of both air/concrete and concrete/aluminum reflections. They are resulting in four start models. For all start models, the inversion results are equal, indicating that the global minimum was found. The obtained time-zero is fixed in the following steps.

Inversion second step   The second step optimized the concrete permittivity and frequency-dependent conductivity $\mathbf{m2} = [\varepsilon_r, \sigma_{fc}, \Delta\sigma]$ by minimizing the misfit between the concrete/aluminum reflection with $\hat{G}_{ca}\hat{W}$, see equations 1.4 and 1.7. As start values for concrete permittivity, a start values average and the result of the first step are used. Start values for σ_{fc}, were 0.05 [S/m] and 0.1 [S/m] and start values for $\Delta\sigma$ were 0.005 and 0.001 [S/m]. The inversion results for these eight start models return similar, less than 1% deviation, medium properties of the concrete slab. This indicates that the global minimum was found.

Inversion third step The third step optimized the concrete permittivity and frequency-dependent conductivity $\mathbf{m3} = [\varepsilon_r, \sigma_{fc}, \Delta\sigma]$ by minimizing the misfit between air/concrete and concrete/aluminum reflections and $(\hat{G}_{ac} + \hat{G}_{ca})\hat{W}$, see equations 1.4 and 1.7. As start values for concrete permittivity, 0.9, 1.0 and 1.1 times the obtained permittivity of step 2 were used. As start values for σ_{fc} and $\Delta\sigma$, 0.5, 1.0 and 1.5 times the obtained σ_{fc} and $\Delta\sigma$ values of step 2 were used. The inversion results for all these 27 start models returned similar medium properties of the concrete slab, which were close to the inversion results obtained in the second step. This indicates that the global minimum was found. Figure 1.9, shows for all specimens the measured data in blue and the inverted data in red. The phase and amplitude spectra in frequency domain are similar and the fit is optimal around the centre frequency fc = 1.2 [GHz]. The time-domain results show air/concrete reflection and concrete/aluminum reflections, which are as well similar. Although the concrete/aluminum reflection inversion gives a better fit in shape and amplitude than the air/concrete reflection. The similarity between the measurements and inverted data indicate that the inversion results describe well the measurements.

1.7 Results

Full-waveform inversion assessment The following discussion focuses on inversion results of both reflections using the 0.575-2.1 [GHz] frequency range. This is also valid for the inversion step of the concrete/aluminum reflection, since it returned similar results. We present inversion results by plotting the medium properties as a function of the relative humidity and chloride content to investigate their dependency in more detail, see Figure 1.9.

Effect of chloride and moisture on results Figure 1.10(a) shows that for increasing chloride content larger conductivities are obtained, whereas relative humidity has little influence on conductivity values. Figure 1.10(b) shows the obtained relative permittivity as a function of the relative humidity for the different chloride contents. The identical chloride content series shows moderately increasing relative permittivity values for increasing relative humidity. Note the slight increase in relative permittivity for increasing humidity compared to the significant increase in conductivity for increasing chloride content. Figure 1.11(a) shows that conductivity is strongly increasing for increasing chloride content and that the slopes are similar for the three different relative humidities. Figure 1.11(b) shows in general an increase of the inverted relative permittivities for increasing chloride content and relative humidities. Two outliers could be identified that did not follow the trend; specimen 2 (70% relative humidity and 0% chlorides) and specimen 5 (70% relative humidity and 0.4% chloride).

Effect on frequency dependent conductivity Figure 1.13 shows the linear frequency dependent conductivities, equation 1.1, for all inverted specimens, Table 1.1. It is observed that the 1% chloride results (circles) have the steepest slopes and the highest conductivity values. Squares (0.4% chlorides) have intermediates slopes and medium σ values. Finally, triangles (0% chlorides) show the lowest slopes with low σ values.
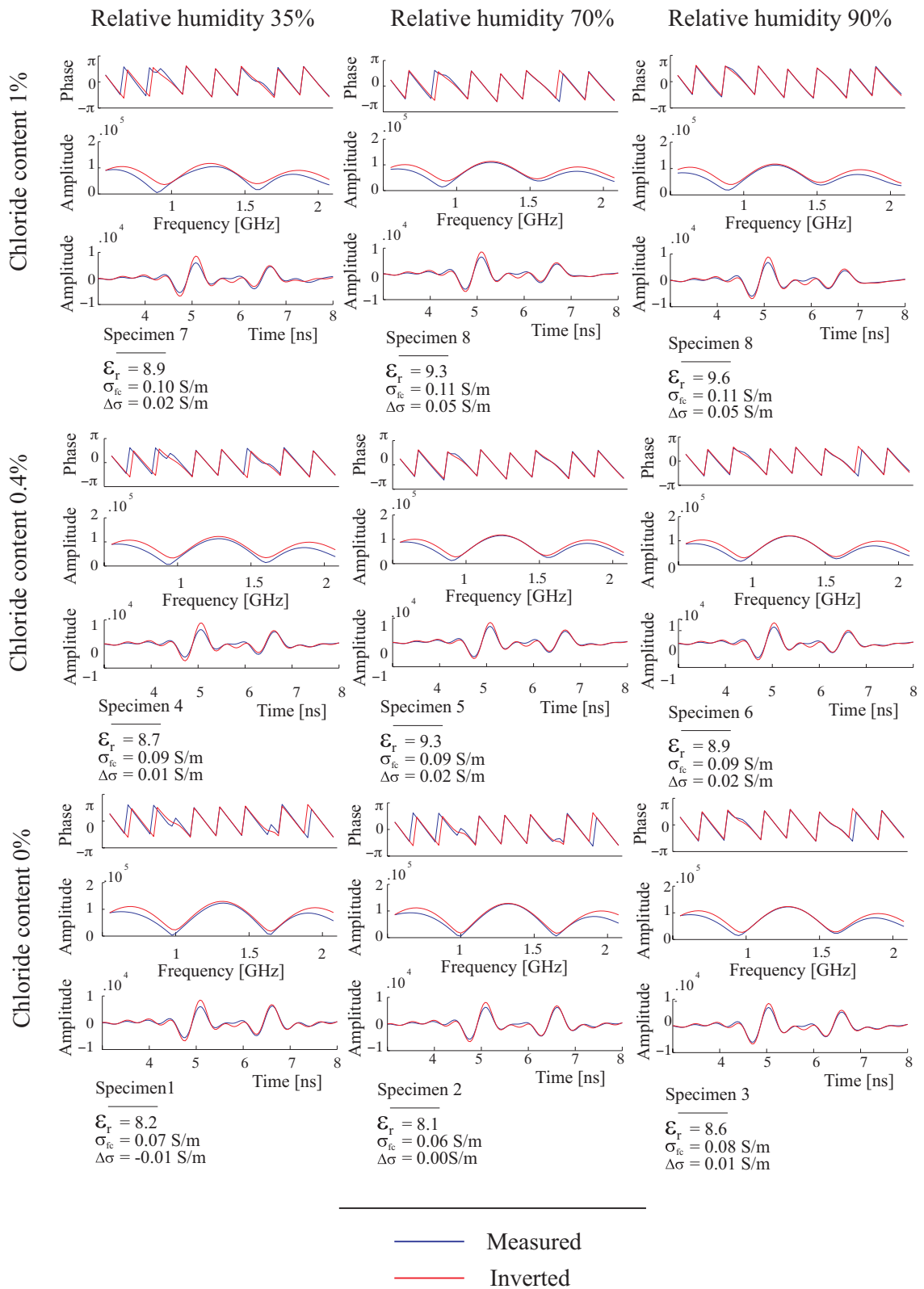
Figure 1.9: Overview of all inversion results using frequencies between 575 [MHz] and 2.1 [GHz]. For each specimen the figure shows the phase (top); amplitude spectrum (middle) in the frequency domain; and signals in the time domain (bottom). They are presented for the measured (blue) and inverted (red) trace.

15
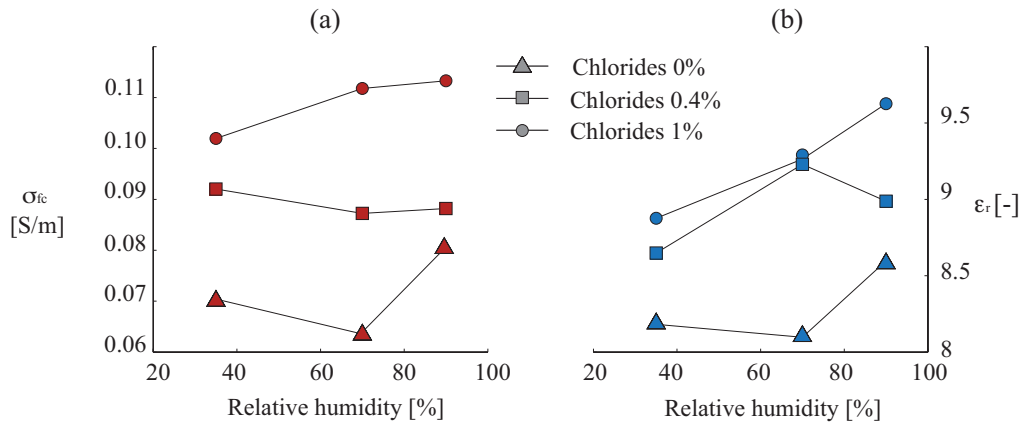
Figure 1.10: (a) Inverted conductivity (σ_{fc}) and (b) permittivity (ϵ_r) values as a function of the relative humidity for different chloride contents.
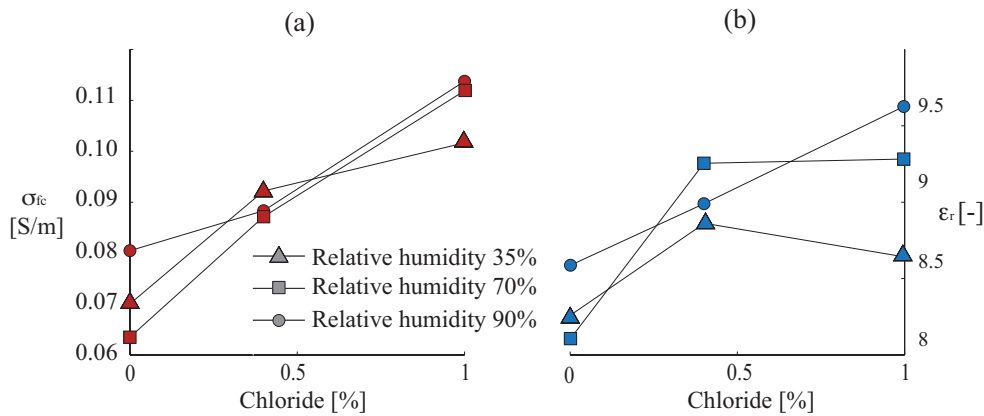
Figure 1.11: (a) Inverted conductivity (σ_{fc}) and (b) permittivity (ϵ_r) values as a function of chloride content for different relative humidities.

Discussion Figure 1.12 shows an overview of all inverted conductivities and relative permittivities for all specimens. The use of three different frequency ranges, indicated by red, grey and blue, provided similar results. This shows the stability of Full-waveform inversion. Again, for increasing chloride and humidity an increasing conductivity and permittivity can be observed, respectively. In this way, both relative humidity and chloride content effects can be observed. This figure shows that the chloride content has a more accentuated effect on conductivity values than relative humidity has on relative permittivity. Moreover, increasing chloride content has a similar influence as relative humidity on relative dielectric permittivity values. This indicates that chloride content is a more discriminating parameter than relative humidity on electromagnetic wave propagation in concrete.
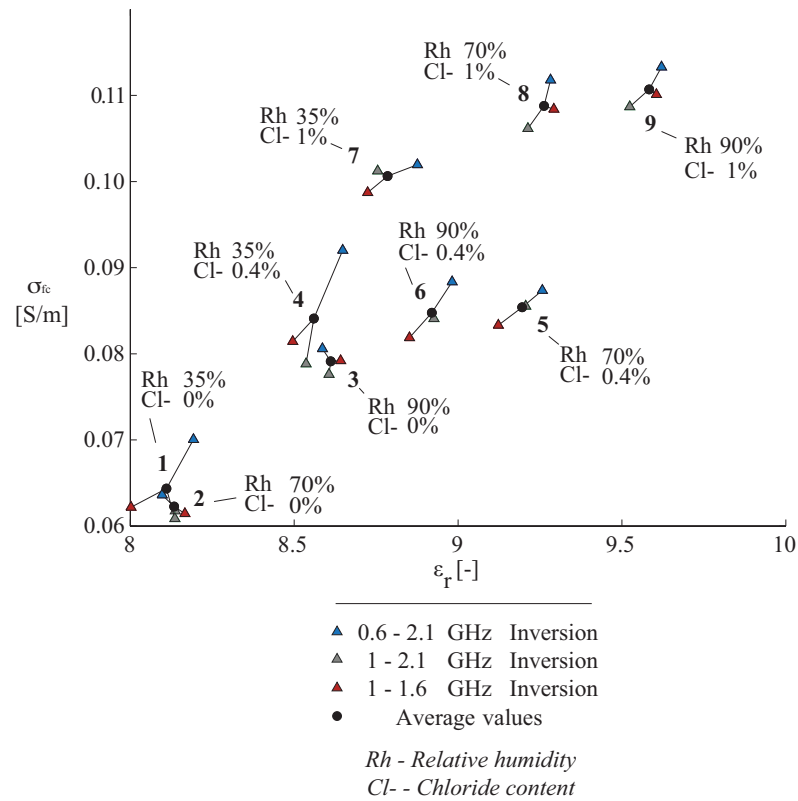
Figure 1.12: Inversion results of frequency dependent conductivities of the specimens, see Table 1.1.
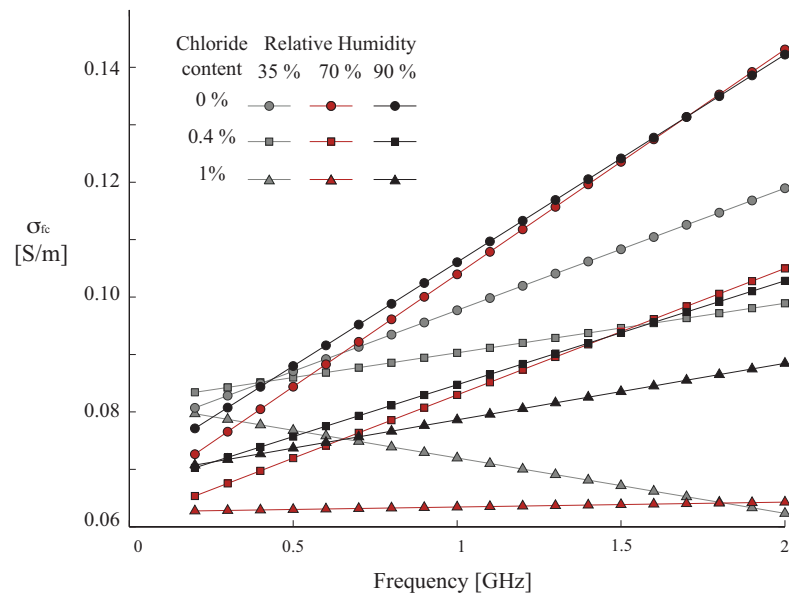
Figure 1.13: Inversion results of frequency dependent conductivities of the specimens, see Table 1.1.

1.8 Conclusions

A novel Full-waveform inversion algorithm was developed for off-ground bi-static GPR horn antennas that uses all information present in GPR traces. Using the full-waveform in the inversion enables the estimation of quantitative electromagnetic properties. The horn antenna GPR system was characterized by estimating the phase centre and the effective wavelet using measurements over a stainless-steel plate. GPR data measured over nine concrete specimens having different moisture and chloride contents were inverted and returned a relative dielectric permittivity and a conductivity that included a frequency-dependent component. The Full-waveform inversion consisted in three consecutive steps. The first inversion step calibrated time-zero using the air/concrete reflection. The second step inverted permittivity and the frequency-dependent conductivity of the concrete using the concrete/aluminum reflection. The third step inverted permittivity and the frequency-dependent conductivity of the concrete bot air/concrete and concrete/aluminum reflections and returned similar results as in the second step. In all steps, several start models were used and returned similar results, which indicates that the inversion was well constrained.

In general, the inversion results show for increasing chloride and humidity content specimens, increasing conductivity and permittivity values, respectively, with the exception of two outliers, specimen 2 and 5. Chloride content has a more accentuated effect on wave propagation than relative humidity. Moreover, for increasing chloride content increasing frequency-dependent conductivity values are obtained. It was shown, that it is possible to discriminate the separate effects of chloride content and relative humidity on both conductivity and relative dielectric permittivity. Future work will focus on, concrete specimens containing different chloride gradients and on the electromagnetic wave propagation model implementation for numerous layers to estimate these gradients.

2 Full-waveform GPR inversion to assess chloride gradients in concrete

Abstract   The spreading of deicing salt on roads during winter exposes reinforced concrete structures to corrosion. Reinforcement corrosion is problematic because it reduces the structure's load carrying capacity and a long-term consequence can be structural failure. The use of Ground Penetrating Radar (GPR) technology is commonly described in literature for reinforced concrete structural mapping. New processing technologies enable the possibility to obtain electromagnetic parameters from GPR data. This paper provides methodologies for the calculation of the electromagnetic parameters from GPR data accounting for chloride content and its distribution within concrete. A GPR dataset was carried out with bi-static off-ground GPR antennas during an experiment recreating chloride contamination processes in concrete specimens. Two novel solutions, using time and frequency domain, are presented in this paper. Their use on the dataset returned the electromagnetic parameters of the concrete specimens with knowledge of their thickness. Firstly, a Time Domain Solution is provided as a light direct computational tool to observe global material properties. Thereafter, a novel Full-waveform inversion based on a multilayered forward model allows identification of the conductivity gradients present inside concrete, is presented. The results, together with additional destructive testing, allowed relation of chloride gradient distribution with concrete specimen electromagnetic parameters.

Johannes Hugenschmidt, EMPA, Switzerland
Jutta Bikowski, Forschungszentrum Jülich, Germany
Jan van der Kruk, Forschungszentrum Jülich, Germany
Eugen Brühwiler, EPFL, Switzerland

Alexis Kalogeropoulos, EMPA, Switzerland
Corresponding Author: alexis.kalogeropoulos@epfl.ch

2.1 Introduction

Motivation   Road bridges can be exposed to reinforcement corrosion due to salt spread in winter for deicing. Steel reinforcement corrosion reduces the bridge resistance and a long-term consequence may be a structural failure. Ground Penetrating Radar (GPR) technology is proposed to assess this problem as it enables the continuous non-destructive evaluation of reinforced concrete elements, see Hugenschmidt & Kalogeropoulos, 2006, [16]; Dérobert *et al.*, 2008, [8]. Previous studies described that permittivity and conductivity values of datasets from electromagnetic coaxial transmission devices changed with concrete specimens water and chloride ion content, Robert 1998 [32], Soutsos *et al.*, 2001[37]. In, Hugenschmidt & Loser 2007 [15], it was observed that amplitudes of GPR pulses reflections are influenced by both the chloride and moisture content. Recently, in Kalogeropoulos *et al.* 2011 [18], it was shown, processing Hugenschmidt & Loser 2007 [15] dataset with a full-waveform inversion, that chloride ions and moisture content have an influence on both permittivity and conductivity results. However, in the concrete specimens used in this dataset, chlorides were added to the mixtures by dissolving NaCl in the mixing water. This had for consequence to have chloride ions homogeneously distributed inside the concrete specimens and not concentrated within the electrolytic solution present inside concrete pores. In real cases, chlorides are distributed in gradients, within the electrolytic solution present inside the concrete pores, over the element thickness due to capillarity and diffusion processes caused by atmospheric conditions, see Conciatori 2005 [6] and appendix III.

Scope   This chapter presents methodologies for the calculation of the electromagnetic parameters accounting for chloride content and distribution inside a concrete slab. A specific experiment enabled the controlled generation of three concrete specimens having different chloride gradients. This was done applying a saline solution on one side of the specimens, once concrete was cured. In this paper, two GPR processing methodologies, enabling chloride content determination, are developed to provide an assessment tool for structural engineers. The GPR dataset was processed using time and frequency domain solutions to obtain the electromagnetic parameters of a finite dielectric body such as a concrete slab; of known thickness. Firstly, a ray-based Time Domain Solution to obtain permittivity and conductivity averages was used. Thereafter, the dataset was inverted using an updated Full-waveform model having a defined amount of layers. This procedure, by determining conductivity gradients, allowed the identification of the chloride distribution generated during the experiment within concrete specimens. The electromagnetic parameters describing the propagation of an electromagnetic wave within a dielectric body, assuming it is non-magnetic $\mu_r = 1$, are the relative dielectric permittivity, ε_r and the conductivity, σ. For commodity this paper will refer to ε_r as permittivity. These results are compared with chloride contamination gradient distributions obtained, from the concrete specimens, at the end of the experiment.
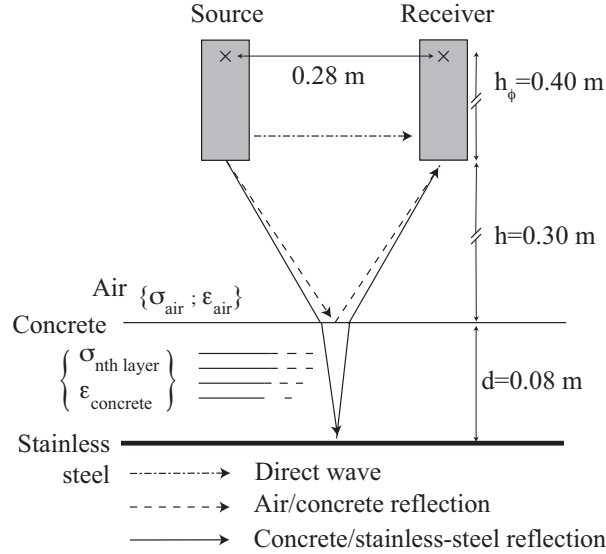
Figure 2.1: GPR measurement setup.

2.2 GPR experimental dataset

The experiment was carried out by measuring a GPR dataset with fixed-height horn antennas above 0.08 m thick slab-like concrete specimens exposed to seasonal chloride contamination cycles, see Chapter 3. To represent real cases a typical bridge deck concrete was used. The cement content was 325 kg/m^3 and the water/cement ratio was 0.5. The concrete specimens were cast in plastic trays and their sides were sealed with a silicon joint. Once cured, the specimens were exposed to chloride ions contamination, placing saline solutions for different durations on the open surface of the specimens, see Table 2.3. A GPR measurement was done at the end of the experiment for each slab, with two off-ground 1.2 GHz horn antennas with a 0.28 m offset. The antennas were placed 0.30 m over the concrete slabs, see Fig. 2.1. A stainless-steel plate, placed at the bottom of the specimens, allowed the assumption that only reflections occurs at this interface. Finally, the concrete specimens chloride contamination gradient distributions were obtained destructively at the end of the experiment, see Figure 2.10.

2.3 Electric field expressions for horizontal medium: multi-layer and layer cases

The modeling as described in Kalogeropoulos *et al.* 2011, [18] is extended to multi-layer case which enables the analysis of conductivity gradients. This section describes the exact expression of the electric field variation induced by a GPR pulse within a horizontally layered medium. The solution is presented in horizontal wavenumber-frequency (f-k) and uses Green's functions to describe the medium. The multi-layer case is presented and from it a

simplified expression is given for a layer case, as it was used in [18]. In f-k domain the expression for the electric field $\tilde{E}_x$ variation generated by a source current, $\tilde{J}(x)$, is decribed in van der Kruk *et al.*, 2006, [39], using:

$$\tilde{E}_x = \left[\tilde{G}_{xx}^{TE} + \tilde{G}_{xx}^{TM} \right] \tilde{J}(x). \tag{2.1}$$

The Green's functions of the electric field $\tilde{G}_{xx}^{TE}$ and magnetic field $\tilde{G}_{xx}^{TM}$ are used to decompose the electric field into up- and down- going TE and TM modes. The Green's function $\tilde{G}_{xx}^{TE}$ consists of the direct wave,

$$D_0^{TE} = \frac{k_y^2 \zeta_0}{2\Gamma_0 k^2} e^{-\Gamma_0(z^r - z^s)}, \tag{2.2}$$

and the reflections; they are calculated recursively with,

$$R_{ab}^{TE} = \left(r_{ab}^{TE} + \frac{t_{ba}^{TE} R_{b(b+1)}^{TE} t_{ab}^{TE} \beta}{1 - R_{b(b+1)}^{TE} r_{ba}^{TE} \beta} \right) e^{-\Gamma_a(z^r + z^s)}, \tag{2.3}$$

where subscripts a and b (a < b) represent the different layers and can take values {0, 1, 2, ..., n}. Waves propagate within the layer indicated by the first subscript and are transmitted into, or reflected at, the layer indicated by the second subscript, see Figure 2.2. The conversion, from f-k to frequency domain follows the equations in van der Kruk *et al.*, 2006, [39]; except that the numerical integration was done with an ϵ extrapolation algorithm. $\tilde{G}_{xx}^{TE}$ and $\tilde{G}_{xx}^{TM}$ are calculated similarly with :

$$r_{ab}^{TE} = \frac{\zeta_b \Gamma_a - \zeta_a \Gamma_b}{\zeta_b \Gamma_a + \zeta_a \Gamma_b}, \; r_{ba}^{TE} = -r_{ab}^{TE}, \tag{2.4}$$

and

$$t_{ab}^{TE} = \frac{2\zeta_b \Gamma_a}{\zeta_b \Gamma_a + \zeta_a \Gamma_b}, \; t_{ba}^{TE} = 2 - t_{ab}^{TE}. \tag{2.5}$$

Where,

$$\beta = e^{(-2\Gamma_a d)}, \tag{2.6}$$

$$\Gamma_a = \sqrt{\gamma_a^2 + k^2}, \tag{2.7}$$

$$\gamma_a = \sqrt{\eta_a \zeta_a}, \tag{2.8}$$

$$\eta_a = \sigma_a + j\omega \varepsilon_a \varepsilon_0, \tag{2.9}$$

$$\zeta_a = j\omega \mu_a, \tag{2.10}$$

$$\omega = 2\pi f, \tag{2.11}$$

z^s and z^r are source and receiver heights, respectively,

$$k_x \text{ and } k_y \text{ the horizontal wavenumbers,}$$
$$d = \text{layer thickness,}$$
$$f = \text{frequency,}$$
$$\varepsilon_a = \text{permittivity,}$$
$$\sigma_a = \text{conductivity,}$$
$$\mu_a = \text{magnetic permeability,}$$
$$\varepsilon_0 = \text{air absolute permittivity,}$$

In *Multi-layer case*, the expression of the Green's function $\tilde{G}_{xx}^{TE}$ of a multi-layered dielectric is:

$$\tilde{G}_{xx}^{TE} = D_0^{TE} + \frac{k_y^2 \zeta_0}{2\Gamma_0 k^2} \left(R_{(n-1),n}^{TE} \right) e^{-\Gamma_0 (z^r + z^s)}, \tag{2.12}$$

where,

$$R_{(n-1),n}^{TE} = \frac{r_{(n-1),n}^{TE} + t_{(n-1,n)}^{TE} R_{n,(n+1)}^{TE} t_{n,(n-1)}^{TE} \beta}{1 - R_{n,(n+1)}^{TE} r_{n,(n-1)}^{TE} \beta}, \tag{2.13}$$

and

$$R_{n,(n+1)}^{TE} = r_{n,(n+1)}^{TE} = -1. \tag{2.14}$$

Recursion starts from the lowest reflector, the concrete/stainless steel interface, using eq. (2.14). In this model, D_0^{TE} was set to 0 because the direct wave was removed during preprocessing. Similarly $\tilde{G}_{xx}^{TM}$ is given.

In the *single layer case*, the multiple reflections generated by the upcoming wave reflection on the upper layer boundary are assumed to be negligible. The term $R_{12}^{TE} r_{10}^{TE} \beta$ that defines this reflection, in eq. 2.12 was set to zero. In this case the concrete/stainless-steel reflection coefficient is expressed with $R_{12}^{TE} = r_{12}^{TE} = -1$. This leads to the expression of the Green's function $\tilde{G}_{xx}^{TE}$ of a single layer medium:

$$\tilde{G}_{xx}^{TE} = D_0^{TE} + \frac{k_y^2 \zeta_0}{2\Gamma_0 k^2} \left[r_{01}^{TE} + t_{01}^{TE} r_{12}^{TE} t_{10}^{TE} \beta \right] e^{-\Gamma_0 (z^r + z^s)}, \tag{2.15}$$

similarly $\tilde{G}_{xx}^{TM}$ is given.

2.4 Average values of ε_r and σ using Time Domain Solution

Time Domain Solution   In order to optimize a real case dataset processing a light computational direct analysis was built. This analysis calculates average values of permittivity ε_r and conductivity σ, see Chap 4. The analysis requires the identification of the positive peaks in the GPR datasets. These peaks are the maximum of each reflection coming from the horizontal interfaces of a dielectric body. Each peak is defined by a time and an amplitude value, Figure 2.4. The equations are expressed for a single-layer configuration and the gradient distribution of chloride ions is not taken into account such that the method calculates average values.

Source Receiver

$\tilde{E}_x = \tilde{J}(x)$

0

1

2

n

Stainless steel

n+1

d_n Γ_n

$\tilde{E}_x = \left[\tilde{G}_{xx}^{TE} + \tilde{G}_{xx}^{TM}\right].\tilde{J}(x)$

$\tilde{G}_{xx}^{TM}$ is calculated similarly

$$\tilde{G}_{xx}^{TE} = D_0^{TE} + \frac{k_y^2 \zeta_0}{2\Gamma_0 k^2}\left(R_{(n-1),n}^{TE}\right)e^{-\Gamma_0(z^r+z^s)}$$

Recursion

$$R_{(n-1),n}^{TE} = \frac{r_{(n-1),n}^{TE} + t_{(n-1,n)}^{TE} R_{n,(n+1)}^{TE} t_{n,(n-1)}^{TE}\beta}{1 - R_{n,(n+1)}^{TE} r_{n,n-1}^{TE}\beta}$$

$$R_{n,(n+1)}^{TE} = r_{n,(n+1)}^{TE} = -1$$
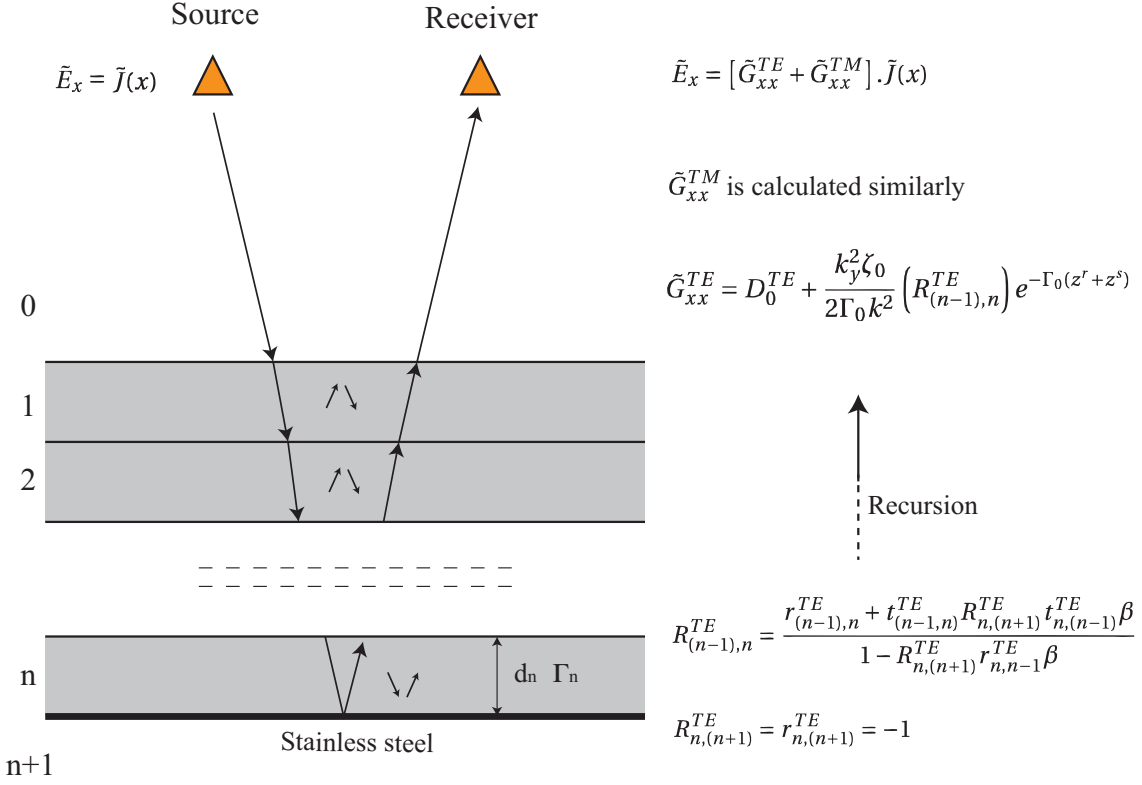
Figure 2.2: Multi-layer model.

Source Receiver

$\tilde{E}_x = \tilde{J}(x)$

0

1

2

Stainless steel, $r_{12}^{TE} = -1$

d_1 Γ_1

$\tilde{E}_x = \left[\tilde{G}_{xx}^{TE} + \tilde{G}_{xx}^{TM}\right].\tilde{J}(x)$

$\tilde{G}_{xx}^{TM}$ is calculated similarly

$$\tilde{G}_{xx}^{TE} = D_0^{TE} + \frac{k_y^2 \zeta_0}{2\Gamma_0 k^2}\left[r_{01}^{TE} + t_{01}^{TE} r_{12}^{TE} t_{10}^{TE}\beta\right]e^{-\Gamma_0(z^r+z^s)}$$

$$R_{12}^{TE} = r_{12}^{TE}$$
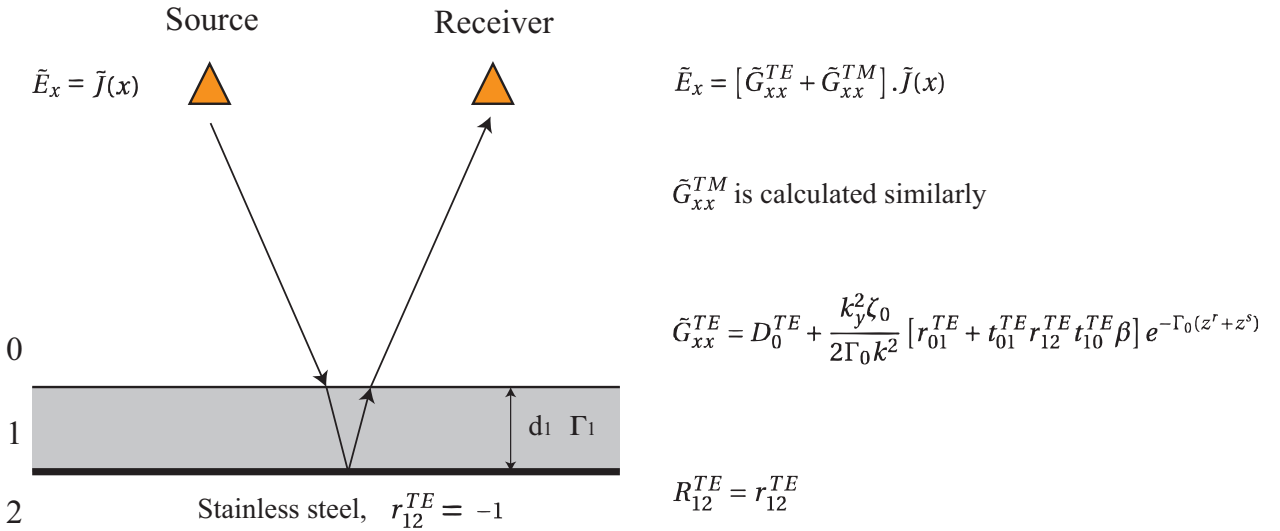
Figure 2.3: Single layer model.
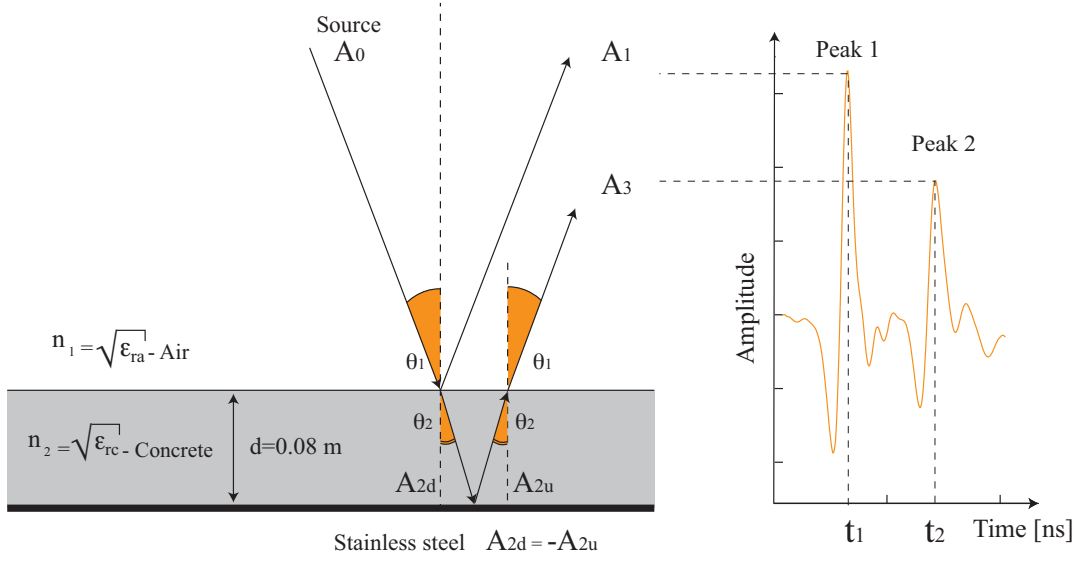
Figure 2.4: Reflections occurring at each interface

Simplifications   Firstly, the frequency independency of ε_r and σ is assumed. Secondly, the antenna offset was not considered, assuming the pulse to propagate vertically, with θ_1 and θ_2 equal to 0, see Figure 2.4.

2.4.1   Relative dielectric permittivity calculation

Combining the dielectric thickness d in [m], with the peaks time position t_1 and t_2, in [ns], gives the velocity v [m/ns], see Figure 2.1.

$$v = \frac{2d}{(t_2 - t_1)}. \tag{2.16}$$

Where $2d$ takes into account the two-way travel distance. From laws of electromagnetism we know that:

$$v = \frac{c_0}{\sqrt{\varepsilon_r}}. \tag{2.17}$$

With the electromagnetic wave velocity in vacuum $c_0 = 0.3$ m/ns. Then inserting 2.16 in 2.17 we obtain the permittivity ε_r [-] of the dielectric:

$$\varepsilon_r = \left(\frac{c_0}{2d} (t_2 - t_1) \right)^2. \tag{2.18}$$

2.4.2   Conductivity calculation

The combination of Maxwell's equations with Snell-Descartes Law of refraction, provides the following expressions for the amplitudes of the reflections occurring at the interfaces, see Figure 2.4. They are expressed as follows :

$$A_1 = r_{ac} A_0, \tag{2.19}$$

25

and

$$A_3 = -t_{ac}\,t_{ca}\,A_0\,e^{-\alpha 2d}, \tag{2.20}$$

with α the attenuation coefficient and $2d$ the two-way travel distance. The ratio between reflected and transmitted energy at the air/concrete interface is given with Fresnel coefficients, r_{ac}, t_{ac} and t_{ca}, where indices a stand for air and c for concrete.

$$r_{ac} = \frac{A_1}{A_0} = \frac{\sqrt{\varepsilon_{ra}} - \sqrt{\varepsilon_{rc}}}{\sqrt{\varepsilon_{ra}} + \sqrt{\varepsilon_{rc}}}, \quad t_{ac} = \frac{A_{2d}}{A_0} = \frac{2\sqrt{\varepsilon_{ra}}}{\sqrt{\varepsilon_{ra}} + \sqrt{\varepsilon_{rc}}}, \quad t_{ca} = \frac{A_3}{A_{2u}} = \frac{2\sqrt{\varepsilon_{rc}}}{\sqrt{\varepsilon_{rc}} + \sqrt{\varepsilon_{ra}}}. \tag{2.21}$$

Then rewriting eq. 2.20 gives:

$$e^{-\alpha 2d} = -\frac{A_3}{t_{ac}\,t_{ca}.A_0}, \tag{2.22}$$

replacing A_0 by A_1/r_{ac} using eq. 2.19 in eq. 2.22 gives:

$$e^{-\alpha 2d} = -\frac{A_3}{A_1}\frac{r_{ac}}{t_{ac}\,t_{ca}}. \tag{2.23}$$

Then, replacing the Fresnel coefficients using the permittivity expression in eq. 2.21, gives:

$$\alpha = -\frac{1}{2d}\,ln\left(\frac{A_3}{A_1}\frac{\varepsilon_{rc} - 1}{4\sqrt{\varepsilon_{rc}}}\right). \tag{2.24}$$

An expression of the attenuation coefficient α of a non-dispersive pulse is given deriving Maxwell's equations:

$$\alpha = \frac{\sigma}{2\sqrt{\varepsilon_r}}\eta_0. \tag{2.25}$$

With the vacuum impedance, $\eta_0 = 377\,\Omega$ and ε_{rc} equal to the previously calculated relative dielectric permittivity. Inserting 2.24 in 2.25 returns for the conductivity σ of a homogeneous layer:

$$\sigma = 2\frac{\sqrt{\varepsilon_{rc}}}{\eta_0}\left[-\frac{1}{2d}\,ln\left(\frac{A_3}{A_1}\frac{\varepsilon_{rc} - 1}{4\sqrt{\varepsilon_{rc}}}\right)\right]. \tag{2.26}$$

Discussion   This analysis uses time differences and amplitudes ratios and it can be applied directly to raw data. The results are independent of time-zero (t_0) or gain parameters, however, gain must be constant. The assumption of a pulse propagating vertically, used to simplify calculations, have an imprecision of about 3%, see appendix 2. The most important parameter to control is the layer thickness.

2.5 Conductivity gradients determination using Full-waveform inversion

Full-Waveform inversion This method was developed with the objective of identifying the chloride ion gradient distributions within concrete specimens. This analysis solves an inverse problem, it minimizes the difference in frequency domain between measured and modeled data. It requires preprocessing steps and the constitution of an accurate forward model taking into account multiples present within the multi-layer case. The concrete specimens have two horizontal interfaces, consequently, GPR data will contain two reflections. The top reflection occurs at the air/concrete interface and the bottom reflection at the concrete/stainless-steel interface, Fig.2.1. In this study, three cases are presented:

* The inversion of the air/concrete surface reflection providing ε_r and σ values that account for the concrete specimens top surface condition.

* The inversion of the concrete/stainless steel interface reflection providing average ε_r, σ and frequency dependent conductivity ($\Delta\sigma$) values that account for the concrete specimens average condition.

* The inversion of the full waveform, containing both reflections, providing average ε_r and gradient σ values that account for the concrete specimens chloride ion distributions.

2.5.1 Preprocessing

The dataset had to be preprocessed for the inversion to take into account GPR measurement configuration.

Gain removal To enhance display and avoid data clipping, due to the different types of reflectors, adapted gain values were given to the recorded traces while measuring. These gain values were removed once the trace was recorded.

Direct wave removal A direct wave is present in the original data; it is emitted by the transmitter and propagates directly to the receiver, see Fig. 2.1. The direct wave signal is mixed with the reflections coming from the specimen's surface. The direct wave was removed using a reference measurement, having the same length 15 [ns] and number of samples 1024, containing no reflections.

Phase centre estimation The phase centre is the virtual point from which the electromagnetic waves seem to be emitted or received. To estimate the phase centre, assuming point source and receiver antennas, a calibration was performed by measuring the reflections coming from a metal plate for heights varying between 0.1 < h < 0.65 [m], see Chapter 1.

Effective wavelet   The effective wavelet describes the pulse that is emitted and received by the antennas. Since the wavelet is unknown it has to be estimated. To reconstruct this wavelet a reference GPR measurement was performed with a stainless-steel plate placed on the specimen's open surface. Then the effective wavelet was extracted by spectral division of the reference measurement:

$$\hat{W}(f) = \frac{\hat{E}_{ref}(f)\hat{G}^{as*}(f)}{\hat{G}^{as}(f)\hat{G}^{as*}(f) + 10^{-10}},$$

(2.27)

where $\hat{E}_{ref}(f)$ is the reference trace with corresponding height, $h + h_\phi = 0.70$ [m], used in dataset inversion. The value 10^{-10} is used to avoid division by zero. The air/stainless-steel Green's function $\hat{G}^{as}$ describes the total reflection, using a reflection coefficient of -1, of a wave propagating from the source to the stainless-steel plate and its back propagation to the receiver, see Chapter 1. Finally, the antennas are drifting in time and can present significant changes in t_0. To take into account this effect, a reference measurement had to be carried out prior recording each trace on concrete specimens. Then a wavelet extraction was performed for each reference GPR measurement. During inversion each trace was inverted with its corresponding wavelet.

Time zero positioning   A correction for t_0 is needed since a stainless steel plate was placed on the specimens top surface for effective wavelet extraction, which slightly changes the vertical location of the reflector. A preliminary inversion procedure is carried out to correct this effect. The correction is generally in the order of 0.001[ns].

2.5.2   Medium properties

Dispersion   In this study, the permittivity is frequency independent within the selected frequency range 800 [MHz] to 2.85 [GHz], a conservative transition frequency $f_t = 450$ [MHz] is calculated in Appendix I.

Frequency dependent conductivity   Conductivity, σ, is the capacity of a lossy dielectric to conduct electrical currents, it influences electromagnetic wave damping. In Chapter 1, Figure 1.6, presents normalized frequency spectrums of GPR measurements. It was observed that when chloride content increases, high frequencies were more attenuated than low frequencies. Hence, conductivity appears to be frequency dependent. Previous works also suggested the presence of a frequency dependent conductivity, see Robert, 1998, [32]; Soutsos *et al.*, 2001, [37]; Lambot *et al.*, 2004, [28]. To include this frequency-dependent conductivity in the desired model the following linear relation was used:

$$\sigma(f, \sigma_{f_c}, \Delta\sigma) = \sigma_{f_c} + \frac{f - f_c}{f_c}\Delta\sigma.$$

(2.28)

Where f_c is the centre frequency of the GPR system (1.2 GHz), σ_{f_c} is the reference electric conductivity at the centre frequency in [S/m] and $\Delta\sigma$ is the frequency dependent conductivity coefficient in [S/m] of $\sigma(f)$. More details can be found in Appendix I.

2.5.3 Forward models

The forward models use Green's functions expressing, in frequency domain, ε_r and σ with the propagation of an electromagnetic pulse in media and the reflections produced at horizontally layered interfaces. The forward models are based on the product in frequency domain of the effective wavelet $\hat{W}$ and the Green's function $\hat{G}$, van der Kruk *et al.* 2006, [39]. In these models the antennas are considered as point sources. The modeled electric field expression of one reflector, $\hat{E}_{model}(f)$, is in the frequency domain, for air/concrete reflection:

$$\hat{E}_{model}(f) = \hat{G}_{ac}(f, \varepsilon_r, \sigma).\hat{W}(f), \tag{2.29}$$

and for concrete/stainless-steel reflection:

$$\hat{E}_{model}(f) = \hat{G}_{cs}(f, \varepsilon_r, \sigma, \Delta\sigma).\hat{W}(f). \tag{2.30}$$

A medium composed of a constant permittivity and having conductivity layers, going from top to bottom interfaces, is used to model the chloride ions gradients between concrete specimens interfaces, with equation 2.12. To minimize calculation resources conductivity was considered frequency independent and changing linearly from top to bottom interfaces. The number and size of the layers is user-defined, 8 layers of 0.01 [m] each were used. In this setup, the wavelet has a wavelength $\lambda_W \approx 0.04$ [m], Rayleigh's criterion wavelength is then 0.04/2 [m], hence $\lambda_{Rayleigh} \approx 0.02$ [m]. The distance between gradient layers is smaller than Rayleigh's criterion wavelength, 0.01 [m] $< \lambda_{Rayleigh}$. In this way no reflections occurs at the conductivity boundaries present in the dataset, as they interfere one with another.

2.5.4 Inversion

The inversion is based on the minimization of a cost function, that relates the misfit between original and model data. The minimization procedure uses the simplex method Lagarias *et. al*, 1998, [25]. The cost function (2.31) is built likewise; the model parameters **m** describe the wave propagation within the concrete slab. The frequency range goes from 800 [MHz] to 2.85 [GHz].

$$C(\mathbf{m}) = \sum_{i=1}^{n} \frac{|\hat{E}_{Data} - \hat{G}(f_i, \mathbf{m})\hat{W}(f_i)|}{n} \tag{2.31}$$

In the following section, the structure of the inversion is presented using specimen 1_1 GPR measurement. The inversion was performed on three cases, the inversion of the top surface reflection corresponding to air/concrete interface, the inversion of the bottom surface reflection corresponding to concrete/stainless-stell interface and the inversion of the full waveform containing both reflections. The trace corresponds to high conductivity and permittivity values of the dataset, see chap 3. Each reflection within the trace is first regarded independently, then the full-waveform was considered.
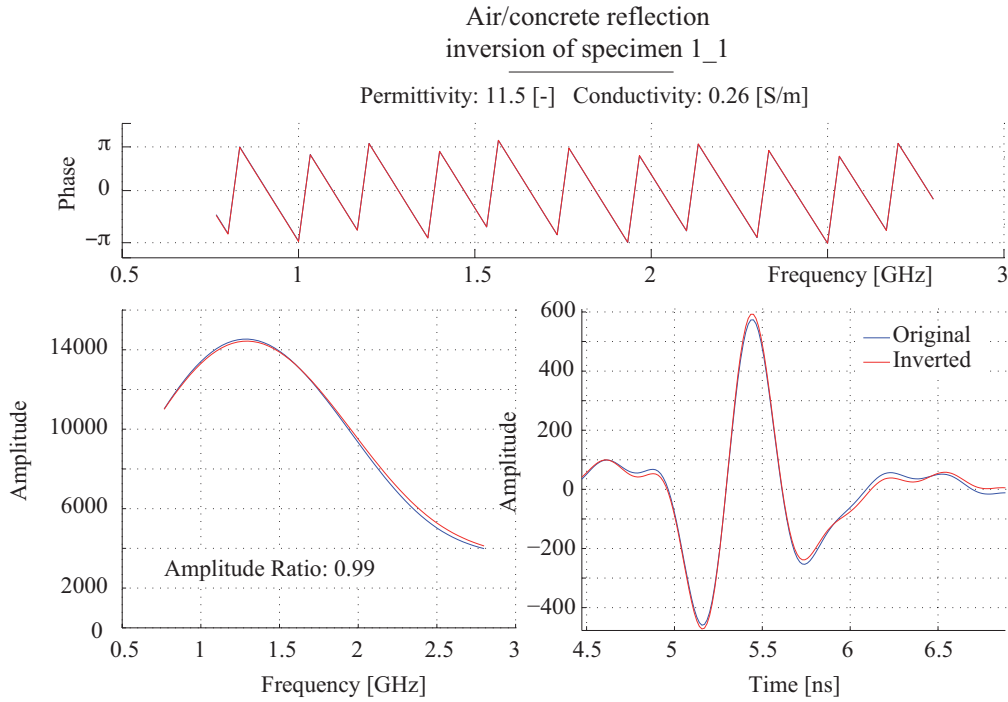
Figure 2.5: Inversion assessment of air/concrete reflection present in the recorded trace giving the EM parameters of concrete top surface. Specimen 1_1 was exposed to 165 [g/l] saline solution for 56 days, see Table 2.3.

Air/concrete reflection inversion   accounts for the pulse propagating in air and its reflection on the external surface of the concrete specimen. Values of ε_r and σ of the slab's first centimeters are returned from this inversion. Values of ε_r and σ calculated with from Time Domain Solution were assigned as start values to the model. Then the misfit between the measured air/concrete reflection and $\hat{G}^{ac}\hat{W}$ was minimized using eq. 2.29 in eq. 2.31. The fit of the reflection is accurate as time domain waveform, phase and spectral density spectrum are overlapping, see, Figure. 2.5.

Concrete/stainless-steel reflection inversion   accounts for the electromagnetic properties of a pulse propagating within a 0.08 m thick concrete slab and having 100% reflection on the bottom surface of it. Values of ε_r, σ and $\Delta\sigma$ returned from the inversion stand for average concrete slab condition. Values of ε_r and σ calculated with from Time Domain Solution were assigned to the model, as start parameters. Then $\hat{G}^{cs}\hat{W}$ is minimized using eq. 2.30 & 2.31. The fit is of an average quality as phases and waveforms are not overlapping properly in fig.2.6.

Full-waveform inversion   Here, the conductivity gradient model was used. Both reflections were considered, in this way accounting not only for the top and bottom reflection but also for the conductivity gradient between them. They were minimized using eq. 2.31 and returned one average value of ε_r, one value corresponding to top surface conductivity σ_{top} and

Concrete/stainless steel reflection
inversion of specimen 1_1

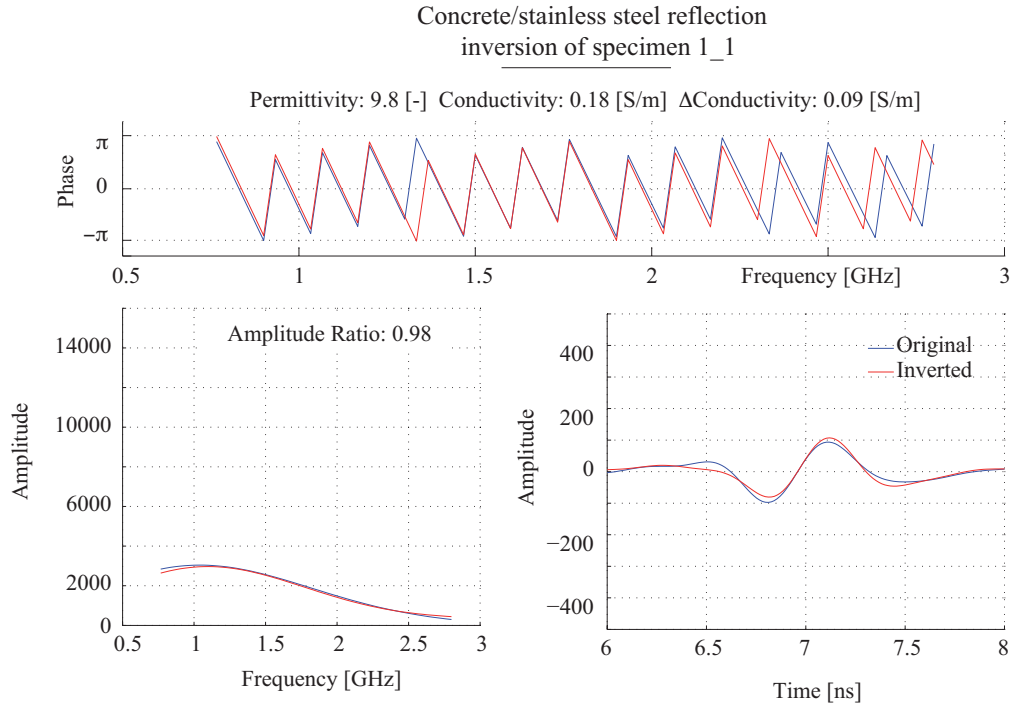Permittivity: 9.8 [-] Conductivity: 0.18 [S/m] ΔConductivity: 0.09 [S/m]

Figure 2.6: Inversion of the second reflection present in the recorded trace giving the average EM parameters from specimen 1_1. The model takes into account frequency dependent conductivity.

one value corresponding to bottom surface conductivity σ_{bot}. Figure 2.7 shows that the minimization of the phase is good, but amplitude and time domain present some error. It appears here, like in concrete/stainless-steel reflection inversion (Fig. 2.6), that the bottom reflection is less well described by the model that the one from top of specimens.

2.6 Assessment with synthetic data

The methods were assessed using the following procedure. Three different synthetic traces were generated using the conductivity gradient forward model and one previously recorded effective wavelet, see eq. 2.27, and Chapter 1. All traces present the same average permittivity and conductivity; ε_r=10.2 [-]and σ= 0.23 [S/m]. Their difference lies within the conductivity gradient distribution, see Table 2.1. Then the electromagnetic parameters of these synthetic traces were calculated using Time Domain Solution and Full-waveform inversion. The first synthetic trace was generated with a constant conductivity to represent the homogeneous case. The second synthetic trace, was modeled using decreasing conductivity gradient from the surface of the slab to its bottom interface, with $\sigma_{top} = 0.44$ [S/m] and $\sigma_{bot} = 0.02$ [S/m]. Finally the last trace is the inverse of the previous case and an increasing conductivity gradient was used with $\sigma_{top} = 0.02$ [S/m] and $\sigma_{bot} = 0.44$ [S/m], see table Table.2.1. The GPR synthetic traces are presented in figure 2.8.

The results displayed in Table.2.1 , indicate that firstly, Time Domain Solution provides re-

Full-waveform inversion
of specimen 1_1

Permittivity: 9.9 [-]   Top Conductivity: 0.27 [S/m] Bottom Conductivity : 0.15 [S/m]

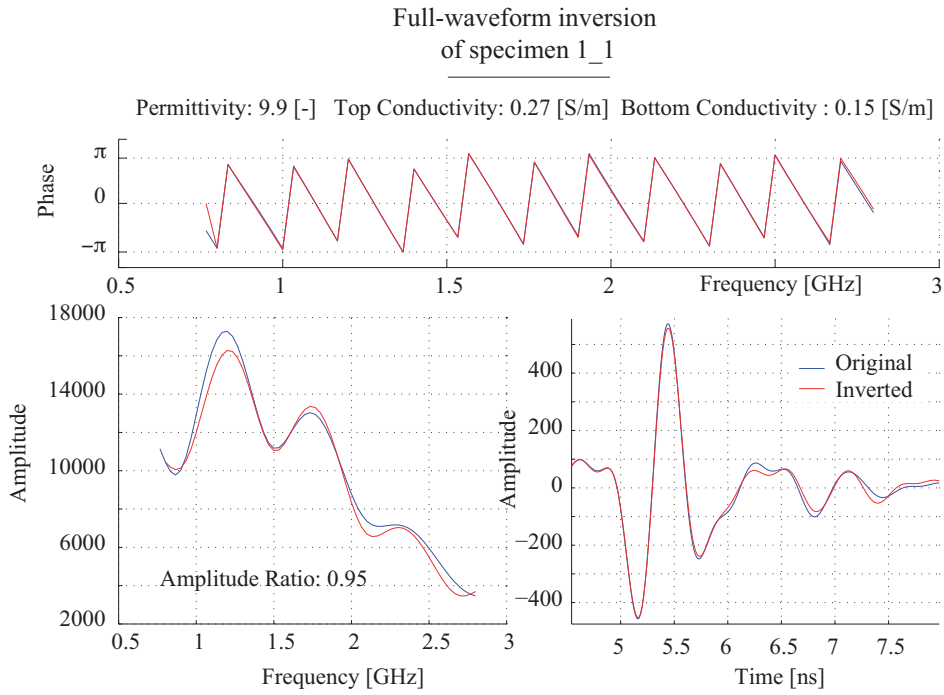Figure 2.7: Inversion of the recorded trace full waveform giving the average permittivity value and the linear conductivity gradient from the top to bottom surface of specimen 1_1 . This inversion is able to determine the presence and the magnitude of conductivity gradients.
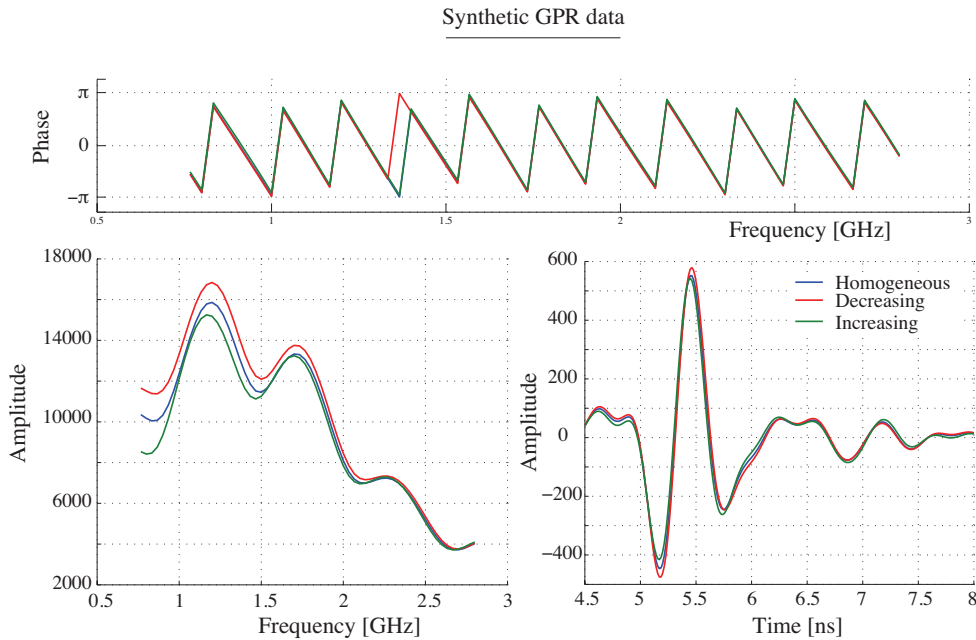
Synthetic GPR data

Figure 2.8: Synthetic GPR data having same average ε_r and σ but different gradient distributions.

Full waveform	Homogeneous	Decreasing	Increasing
ε_r	*10.2* ; 10.2	*10.2* ; 10.2	*10.2* ; 10.2
σ_{top} [S/m]	*0.23* ; 0.23	*0.44* ; 0.44	*0.02* ; 0.02
σ_{bot} [S/m]	*0.23* ; 0.23	*0.02* ; 0.02	*0.44* ; 0.44

Table 2.1: Synthetic gradients assessment (*model* ; result)

Time domain solution	Homogeneous	Decreasing	Increasing
ε_r	10.2	10	10.3
σ [S/m]	0.23	0.24	0.22

Table 2.2: Time domain solution and Full-waveform values obtained using the synthetic gradients during assessment.

sults having a reasonable accuracy, ± 0.15 [-] for ε_r and ± 0.01 [S/m] for σ. Secondly, Full-waveform inversion returns accurate results in the homogeneous case, and is able to identify the gradients. Figure 2.8 shows that the low frequency part of the spectral densities are more attenuated with decreasing σ_{top} and increasing σ_{bot}. The gradient distribution seems to affect also waveforms, but in this conductive case the difference is small as concrete/stainless steel reflection is damped.

With this assessment it is possible to conclude, that Time domain solution provides reasonably accurate average EM parameters calculation. The separate inversion of time domain events brings for each reflection different information. The first reflection inversion returns values for the top surface parameters. Second reflection inversion returns the average condition of the concrete slab. Full-waveform inversion describes the conductivity gradient between top and bottom surface. This procedure is able to identify the conductivity gradients. GPR synthetic conductivity gradients showed differences in the spectral densities plots and some changes in time domain waveforms.

2.7 Results

The GPR dataset was recorded over three concrete specimens that were exposed to different chloride contaminations, see Table 2.3, and Chapter 3. It was processed using Time Domain Solution and Full-waveform inversion. The results are compared with σ values obtained with a Wenner device and chloride contamination profiles of the specimens obtained destructively.

Destructive testing Figure 2.10 gives the chloride % with respect to concrete mass, of 1 cm thick slices, going from the top to the bottom of the specimens. There profiles present similarities in their chloride distributions. The maximum chloride concentration is located at 2 cm below the top surface. This observation was also discussed by, Conciatori, 2005, [6]. Specimen 2_1 has a higher final free chloride content with respect to specimen 1_1 and 2_2. Finally, the presence of increasing chloride ions concentration is observed in last bottom 3

Full-waveform inversion
of specimen 2_1

Permittivity: 10.2 [-] Top Conductivity: 0.32 [S/m] Bottom Conductivity: 0.12 [S/m]

Full-waveform inversion
of specimen 2_2

Permittivity: 9.3 [-] Top Conductivity : 0.25 [S/m] Bottom Conductivity: 0.12 [S/m]
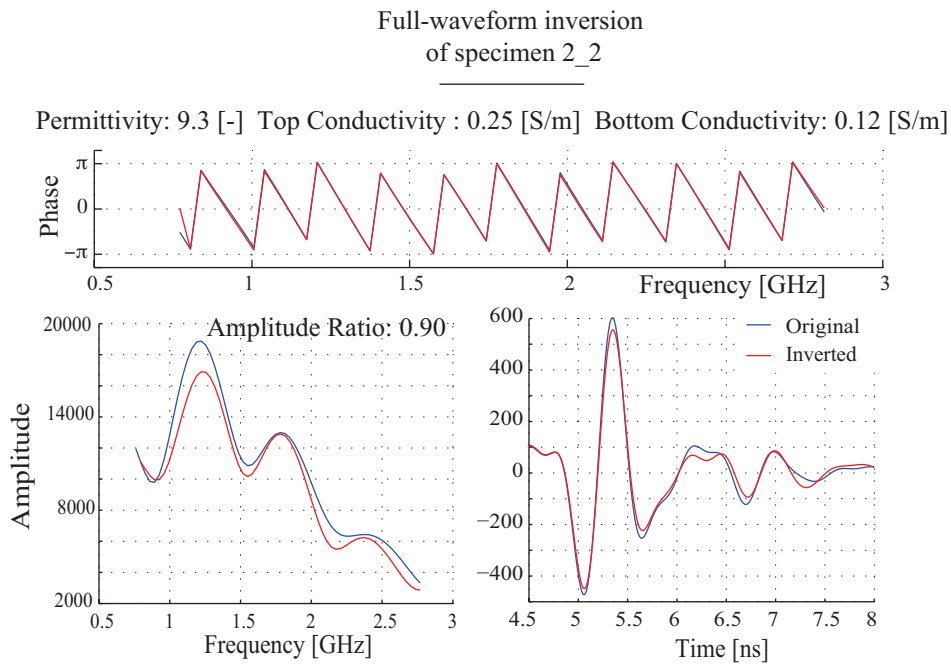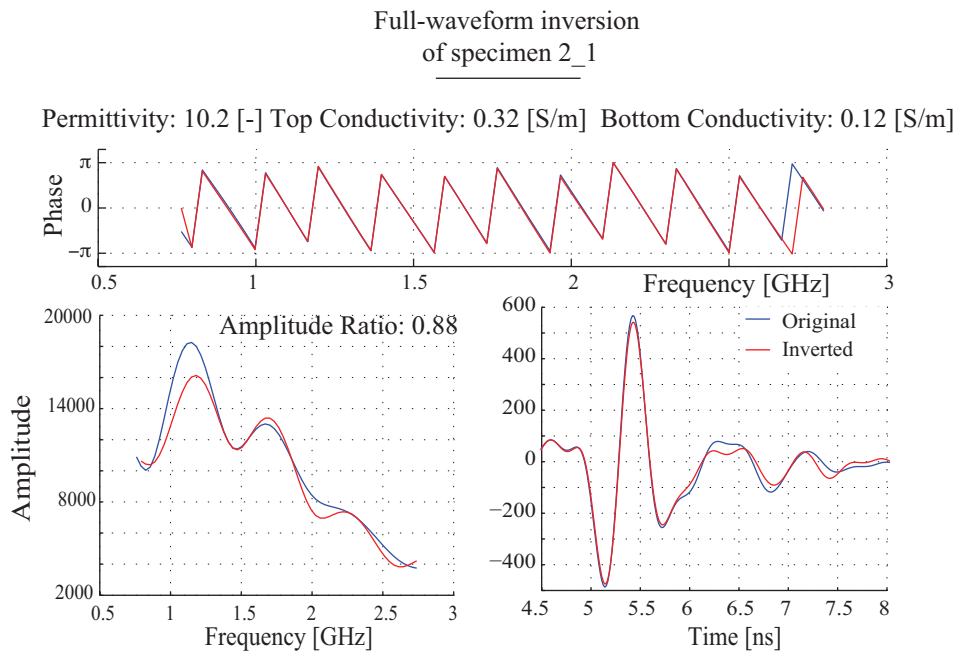
Figure 2.9: Full-waveform inversion results of Specimen 2_1 and 2_2

Tables of results

	Specimen 1_1	Specimen 2_1	Specimen 2_2
Saline solution [g/l]	165	247.5	165
Exposition in days	56	36	157

Table 2.3: Concrete specimen typology

Methodology	Parameter	Specimen 1_1	Specimen 2_1	Specimen 2_2
Time domain	ε_r	10.2	10.7	9.5
solution	σ [S/m]	0.23	0.24	0.20
	ε_r	9.8	10.3	9.1
Concrete/stainless steel	σ [S/m]	0.18	0.18	0.16
reflection inversion	$\Delta\sigma$ [S/m]	0.09	0.13	0.06
Wenner	σ [S/m]	0.24	0.24	0.19

Table 2.4: Table of average values

Methodology	Parameter	Specimen 1_1	Specimen 2_1	Specimen 2_2
Air/concrete	ε_r	11.5	12.9	13.0
reflection inversion	σ_{top} [S/m]	0.25	0.34	0.23
	ε_r	9.9	10.2	9.3
Full waveform	σ_{top} [S/m]	0.27	0.32	0.25
inversion	σ_{bot} [S/m]	0.15	0.12	0.12

Table 2.5: Table of gradients

Figure 2.10: Free Chloride % gradients of all specimens with respect to concrete mass. The gradients are analyzed using slices of 1 [cm] from cores probed on the specimens

cm of all slabs. Specimen 1_1 presents more chlorides at it's bottom that the others. This indicates that the sealing of the 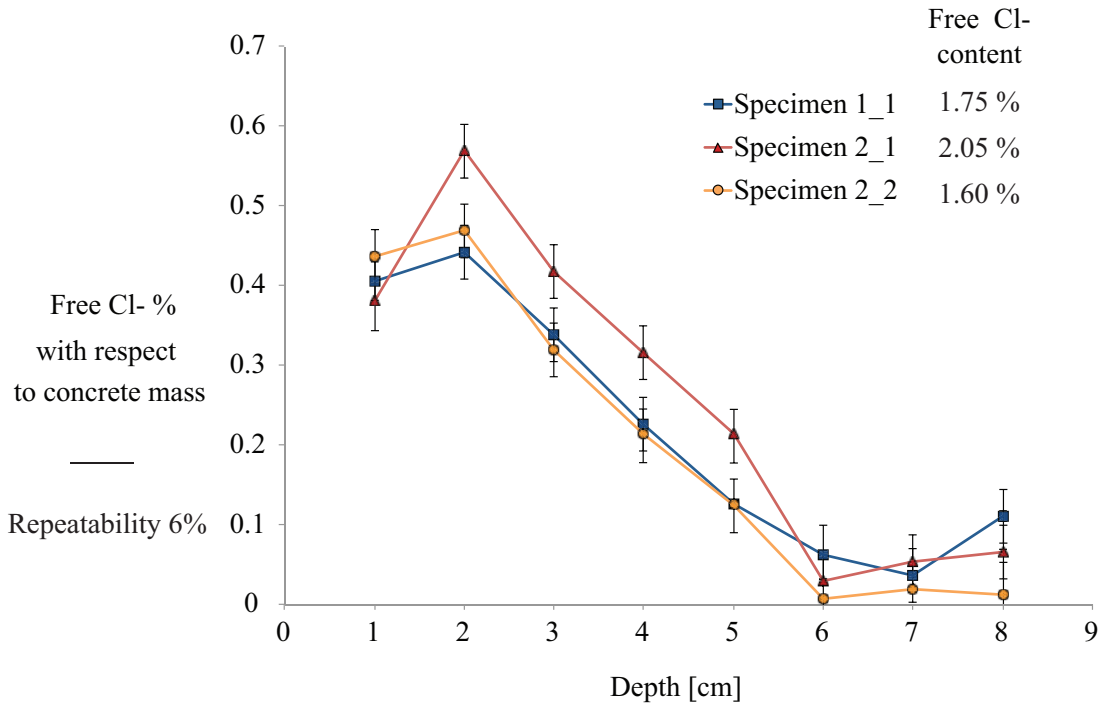side of the specimen was breached and that some saline solution poured on the sides of the specimens and reached the bottom of the slabs.

GPR results for average ε_r and σ The results presented in Table 2.4 can be juxtaposed with free chloride content % of the specimens presented in figure 2.10. Comparing them shows that Time Domain Solution average ε_r and σ values plus the ε_r and $\Delta\sigma$ returned from the concrete/stainless steel reflection inversion increase with chloride ion content, this was also observed in chapter 2, [18]. However, σ from Wenner measurement and σ returned from concrete/stainless-steel reflection inversion present smaller differences. Chapter 3 describes the influence of chloride and water content on average values of ε_r and σ. Finally, the values of ε_r are comparable with the one provided by literature for similar cases, Villain *et al.*, 2009, [40]; Hasar *et al.*, 2009, [14]; Soutsos *et al.*, 2001, [37]; Robert, 1998 [32].

GPR results for average ε_r and σ gradients The results of air/concrete reflection inversion and full-waveform, are presented in Table 2.5. It is observed that the conductivity gradients are consistent with the chloride gradients given in Figure 2.10. Values of σ_{top} returned from air/concrete reflection inversion and with Full-waveform are similar and they increases with chloride content. Similarly with chloride gradients, in figure 2.10, the value of σ_{bot} is more important in specimen 1_1 that in 2_1 and 2_2. Figures 2.7 and 2.9, show the Full-waveform inversion results of all specimens. In all figures time domain and phase fits are accurate,

while amplitude are less well described. The amplitude ratio is the lowest with the more conductive specimen (2_1). Also it is observed that the waveforms are changing with the gradient intensity, particularly when looking at concrete/stainless steel reflections. Finally, even though the conductivity gradients are not exactly representative of ground truth, as they were assumed to be linear, the estimation of chloride ion gradients is correct.

Effect of surface wetness   During the whole experiment prior to GPR measurements the surface of the specimen was dried, using a blowdryer, after the superfluous saline solution was removed. To estimate the influence of the evaporated water, on ε_r and σ, the specimen was weigh prior and after blowdryer use. The difference is 0.14 ±0.02 kg and the specimen weighs around 153 kg. The inversion of the measurement prior to drying returns ε_r = 10.1 [-], σ_{top} = 0.40 [S/m] and σ_{bot} = 0.03[S/m]. The inversion of the measurement after drying, is listed in Table 2.5, and returns ε_r = 9.9 [-], σ_{top} = 0.27 [S/m] and σ_{bot} = 0.15[S/m]. Finally, the average permittivity value ε_r =10.2 [-] and conductivity value σ = 0.24 [S/m], obtained with Time Domain Solution, are similar when compared with specimen 1_1 values after drying. In Table 2.4, the values presented for specimen 1_1 having a dry surface are permittivity ε_r =10.2 [-] and conductivity σ = 0.23 [S/m]. These results indicate that conductivity gradients determination is sensitive to surface condition, while the average EM parameters are little affected by these local changes.

2.8   Conclusions

This paper describes a time and an frequency domain solution providing values of electro-magnetic parameters for horizontally layered concrete slabs. A GPR dataset was obtained with 1.2 [GHz] horn antennas on concrete specimens containing different chloride gradients. Thereafter, the dataset was processed with the following novel methods. Firstly, Time Domain Solution provides average values of relative dielectric permittivity ε_r [-] and conductivity σ [S/m]. Secondly, an extended Full-waveform inversion, based on a multi-layer forward model, enables the creation of conductivity gradients for multi-layered media. The inversion considers also each reflection independently and this provides two different informations. Air/concrete reflection inversion provides values of ε_r and σ from top concrete surface. While inverting the concrete/stainless steel reflection, similarly to Time Domain Solution, provides averages ε_r and σ plus a linear frequency dependent conductivity coefficient $\Delta\sigma$. Finally, the inversion of the full-waveform describes the concrete slab average ε_r and conductivity gradients between top (σ_{top}) and bottom (σ_{bot}) surfaces. The methodology assessment, revealed that Time Domain Solution provides results having a reasonable accuracy, with ±0.15[-] for ε_r and ±0.01 [S/m] for σ. In parallel, the specimens were controlled with another non-destructive technique, the Wenner method. At the end of the experiment, the presence of chloride gradients was measured destructively. The GPR results are matching the ones provided from literature, a different non-destructive device and destructive testing. With it, it is observed that the updated Full-waveform inversion procedure allows the accurate estimation of chloride ion gradients present within concrete. However, some limits are still present within the presented solutions.

Future work will consist of updating the forward model corresponding to the bottom reflection using a different frequency dependent conductivity expression. Time Domain Solution will be updated for a multi-layer case to take into account the presence of an asphalt layer. Finally, both solutions will be applied to real case bridge deck datasets.

Acknowledgment

3 Linking chloride ion concentration in concrete with GPR data

Abstract The spreading of deicing salts on roads produce chloride ions. Salt is commonly used in countries of cold climates for deicing. Also modern bridge decks structures are mostly constructed using reinforced concrete. Chloride ions expose the reinforcement to corrosion by removing, within the concrete, the protecting passivation layer on the steel surfaces. In such conditions, this problem is a major challenge for civil engineers. This paper deals with the non-destructive monitoring of chloride ion concentration inside the concrete of bridge decks, in the case of seasonal exposition to chlorides. An experiment recreating chloride contamination processes in concrete was designed. From it, a Ground Penetrating Radar (GPR) dataset was acquired. Because it is a non-destructive technique, GPR has the advantage, in the case of bridge decks inspection, of mapping the structure without stripping the asphalt layer, nor interrupting traffic. Nowadays, new data processing enables the possibility to obtain values of the electromagnetic (EM) parameters.The relation linking chloride content with EM parameters needs to be known. With it, the combination of the structure's mapping and the corresponding EM parameters can then account for the bridge deck condition plus chloride contamination. This experiment tests the sensitivity of GPR to chloride and moisture seasonal variation in bridge-deck concrete, shows a relationship linking concrete condition and the EM parameters, finally from these relations a threshold, identifying a high probability of corrosion initiation, is deduced. The EM parameters were calculated from the dataset using a novel GPR data processing,Time Domain Solution.

Roman Loser, EMPA, Switzerland
Eugen Brühwiler,EPFL, Switzerland
Johannes Hugenschmidt, EMPA, Switzerland
Jan van der Kruk, Forschungszentrum Jülich, Germany

Alexis Kalogeropoulos, EMPA, Switzerland
Corresponding Author: alexis.kalogeropoulos@epfl.ch

3.1   Introduction

During winter, salt is applied on roads for deicing. When salt crystals reach water mixed with snow and ice, they start to dissolve into chloride Cl- and sodium ions Na+. Their presence in the water lowers the freezing temperature and prevents the melted mixture to freeze again. In this way, bonding between the ice layer and the bridge surface is prevented.

3.1.1   Chloride induced corrosion

The chloride ions dissolved in melt water will progressively pass through the pores and cracks of the asphalt layer. Consequently, saline water will accumulate at the interface between asphalt and concrete and the solution gradually migrates through the concrete pores reaching the reinforcement layer. During drying, water evaporates without mobilizing chlorides that remain inside the concrete. In this way, the seasonal variation causes the chlorides to gradually migrate through the pores of the concrete by capillarity and diffusion processes, see Conciatori, 2005, [6]. As a consequence of these transportation processes it is expected for chloride ions, to be distributed in gradients, within a concrete structure.

Reinforced concrete structures and specifically bridge decks contain several layers of steel reinforcement bars (rebars) for structural resistance. Once chlorides reach the first rebar layer, generally located at 2-4 cm depth, the chloride ions remove the protecting passivation layer on the steel rebar surface and localized corrosion, pitting, initiates. Different studies have shown that the probability of corrosion initiation increases steadily with increasing chloride levels. This probability is considered high, when chloride content exceeds 0.5% of cement mass, see H. Boehni, 2005, [3]. Once initiated, the corrosion process does not stop and the rebars progressively lose their mechanical resistance until possible structural failure.

3.1.2   Concrete electromagnetic parameters assessment using GPR

Ground penetrating radar (GPR) is a non-destructive technique based on the emission and reception of electromagnetic (EM) waves. It produces profiles relating the structure of investigated objects. The profiles are composed of series of measurements along a line. A point of measurement is presented as a trace, which reflects the variation of electric field in time generated by electromagnetic pulses propagating and reflecting within the material. The use of GPR technology is commonly described in literature for reinforced concrete structural mapping, Hugenschmidt & Kalogeropoulos, 2006, [16]; Dérobert *et al.*, 2008, [8]. Because it is a non-destructive technique GPR has the advantage, in the case of bridge decks inspection, to map the structure without the need to strip the asphalt layer nor interrupting the traffic. Recently, ray-based and Full-waveform inversion methodologies brought the possibility to quantify the electromagnetic parameters of the investigated objects.

The electromagnetic parameters ε_r and σ   Maxwell's equations explains how an electromagnetic wave propagates in a non-magnetic dielectric medium. The velocity and the damping that it will experience will vary with the conductivity (σ) and the relative dielectric permittivity (ε_r) of the medium. GPR generates pulses in a domain ranging from 1.10^6 to 5.10^9 [Hz].

Within this bandwidth, Laws of electromagnetism define σ as the capacity of a dielectric to conduct electrical currents. These currents, expressed in Siemens per m [S/m], are produced by the displacement of *charged free particles* inside the dielectric, for instance, dissolved Cl-ions within the solution present inside the concrete pores. The relative dielectric permittivity ε_r is the ratio between dipolar rotational velocity of the *bound charges* constituting the molecules of matter and void. ε_r influences the wave propagation velocity and because it is a ratio, it is unit-less [-]. Each dielectric material has its own ε_r and σ, for instance, air and a concrete slab contaminated with saline water. At each boundary, between two dielectrics, the pulse will separate into a reflected and a transmitted wave. The angle of transmission and reflection plus the proportion between the transmitted and reflected energy are given by Snell's-Descartes Law and Fresnel's coefficients, respectively. For more details see Chapters 1, 2 and Appendix I.

3.1.3   Interest of research

During the last decade, several studies have shown the influence of chloride and moisture on GPR datasets, Hugenschmidt and Loser, 2006, [?]; Robert, 2001, [32]. In Kalogeropoulos *et al.*, 2010, [18], it was shown that chloride and moisture content have an influence on both ε_r and σ. However, in the concrete specimens used in this dataset, chlorides were added to the mixtures by dissolving NaCl in the mixing water. This had for consequence to have chloride ions homogeneously distributed inside the concrete specimens and not concentrated within the electrolytic solution present inside concrete pores. The relations linking ε_r and σ with chloride and water content needs to be investigated. Combined with structure's mapping the EM parameters will account for the bridge deck condition and it's chloride contamination level.

In this paper, it is proposed to test the sensibility of GPR to chloride and moisture seasonal variation in the type of concrete used for bridge decks, and if possible to find a relationship linking concrete condition and the EM parameters. A simplified case was considered, that is the single layer configuration. Where, only the concrete layer is taken into account and no asphalt layer is present on top of it. This is done by, first monitoring concrete specimens exposed to controlled wetting-drying cycles to recreate real case conditions. Then, variations of ε_r and σ are calculated from the dataset using novel Time Domain Solution, see Chapter 2. Finally, the dataset was processed using linear regressions to build a empirical relationships between chloride content, water content, ε_r and σ. From these relations a methodology to deduce a maximum acceptable conductivity at saturation is presented. This value marks the domain where corrosion initiation has a high probability to occur.

3.2   Experimental setup

3.2.1   Concrete specimens

To represent real cases a typical bridge deck concrete was used. The cement content was $325\,[kg/m^3]$ and the water/cement ratio was 0.5. The concrete specimens were cast in plastic trays and their sides were sealed with a silicon joint, see fig. 3.1 (a). The specimens were then

Top view

0.965 m

Concrete reflection

Stainless steel reflection

GPR

Stainless
steel plate

0.75 m

0.81 m

0.9 m

Plastic tray

0.08 m

Concrete

Stainless
steel

0.30 m

Side view

Side view

(a) Specimen design

(b) Measurement setup

(c) Specimen 1_1 experiment timeline

Cycle

First cycle

Second cycle

Curing, 90%
relative humidity

Storage, 70%
relative humidity

Storage, 70%
relative humidity

Stage

Drying, 35%
relative humidity

Chlorides,
specimen is covered

Chlorides,
specimen is covered

Timeline
[days]

0

100

200

300

400

500

600

GPR
measurement

Control specimens
destructive
testing

Experiment specimens
destructive
testing

Figure 3.1: Experimental Setup

exposed to two chloride contamination cycles. Figure 3.1 (c) shows the different stages of cycles and when a GPR measurement was done.

First cycle During the curing stage, all specimens were stored in a 90% controlled relative humidity chamber for 50 days. Thereafter, they were placed 35 days in a 35% relative humidity controlled atmosphere to dry. After this, different saline solutions were placed on the specimen's open surface for different durations, see Table. 3.1. During this operation specimens were covered to avoid evaporation. At the end of this stage, the superfluous chloride solution was removed from the specimen's open surface. Finally, they were stored in a 70% controlled relative humidity chamber for one year, so that, the water present on the specimen's open surface gradually evaporates until stabilization.

Second cycle A second exposure to chloride was applied to the specimens using the same salt concentrations. Similarly to the first cycle, once superfluous water was removed and the specimens were stored back into the 70 % relative humidity chamber to dry.

Chloride content The presence of chloride inside all specimens was confirmed from cores taken at the end of the experiment. The free chloride ions % with respect to concrete mass of the entire cores (8 cm) were tested using a water extraction procedure, see table 3.1. Firstly, with this result it was observed that chlorides are distributed in gradients. Then, that the bottom of the slabs was contaminated with chlorides ; indicating that the specimen's sealing that was supposed to insure impermeability, did not work properly. Consequently, the chlorides present at the bottom of the slab increased the total quantity of chloride inside the concrete specimen. However, this imprecision does not affect this experiment as the analysis is based on average values, chloride distribution inside concrete is thus not considered. In Chapter 2 an extended GPR Full-waveform inversion procedure is presented to estimate these gradients.

3.2.2 GPR measurements

GPR measurements were carried out with two off-ground 1.2 [GHz] horn antennas with an offset of 0.28 [m]. The antennas were placed 0.30 [m] over the concrete slab, see fig. 3.1(b). A stainless-steel plate was placed at the bottom of the specimen, which allowed the assumption that only reflections occurs at this interface. The GPR dataset contained measurements, carried out over all specimens at defined time lapses during each cycle, figure 3.1(c).

Data was processed using Time Domain Solution, see Chapter 2. This analysis estimates average values of the relative dielectric permittivity ε_r and the conductivity σ of a concrete slab. It is based on a model having several simplifications and was developed in order to limit data processing and use little computational resources. This solution answers a direct problem and its most influencing parameter in the calculation of ε_r and σ is the slab thickness, 8 cm in this case. This analysis is relative and it can be applied directly to raw data, however, gain must be constant.

3.2.3   Complementary observations
To confirm and complete the GPR dataset, complementary measurements were performed.

Weighing   First the specimen was weighed after each GPR measurement enabling this way the water content evolution to be monitored, since the mass loss corresponds to evaporated water, see figure 3.2.

Pore size distribution and water content   Secondly, because a difference in porosity can influence water content, the porosity of 5 cores collected on each specimen was tested. The pore size distribution and the dry density are provided. For verification, the percentage of water present inside all specimens was obtained. This was done by storing blocks taken from the specimens in an oven for 60 days; like for mass monitoring the mass loss corresponds to evaporated water. In table 3.2 and 3.3, it is observed that all the tested concrete specimen are comparable with respect to their porosity, density and water content. Hence, they will be comparable with their respective chloride contamination processes, table 3.1.

Total and free chloride content   Finally, to evaluate the presence of Friedel salt binding chloride ions with cement paste, the total Chloride content was obtained. This was done with three cores taken from specimen 1_1 at the end of the experiment. The free and total Cl- content of their top 5 cm was measured using water and acid extraction procedure, respectively. The results show that there are no substantial differences, indicating; first that the specimen is homogeneously contaminated. Second that the free chloride content can be considered equal to total chloride content with less than 0.1 percentage point difference, see table 3.4.

3.3   Results
Weight evolution analysis   Figure 3.2 shows the weight evolution of specimen 1_1 during the experiment. The balance had a precision of 0.02 Kg. It was observed that during curing and drying phases the specimen loses weight rapidly due to water evaporation and during both chloride inoculation stages, weight increases. Finally, it can be observed, that the mass loss during the storage phase is important during first 100 days afterwards the decrease is reaching an asymptotic limit, that is linked to the environment relative humidity.

Time of exposure   Table 3.1, presents the saline solution concentration used for chloride inoculation, the time of exposure, and the final percentage of free chloride ions with respect to concrete mass. It is observed that specimen 1_1 and 2_2, exposed to the same saline solution concentration but to different times of exposure, had little difference with one another. This indicates that, in this setup, time of exposure to saline solution has a small influence on the concrete specimen chloride content.

Evolution of ε_r and σ   Figure 3.3, shows the evolution of average ε_r and σ of specimen 1_1 during the whole experiment. A conservative precision is estimated using ± 0.03 [S/m] for
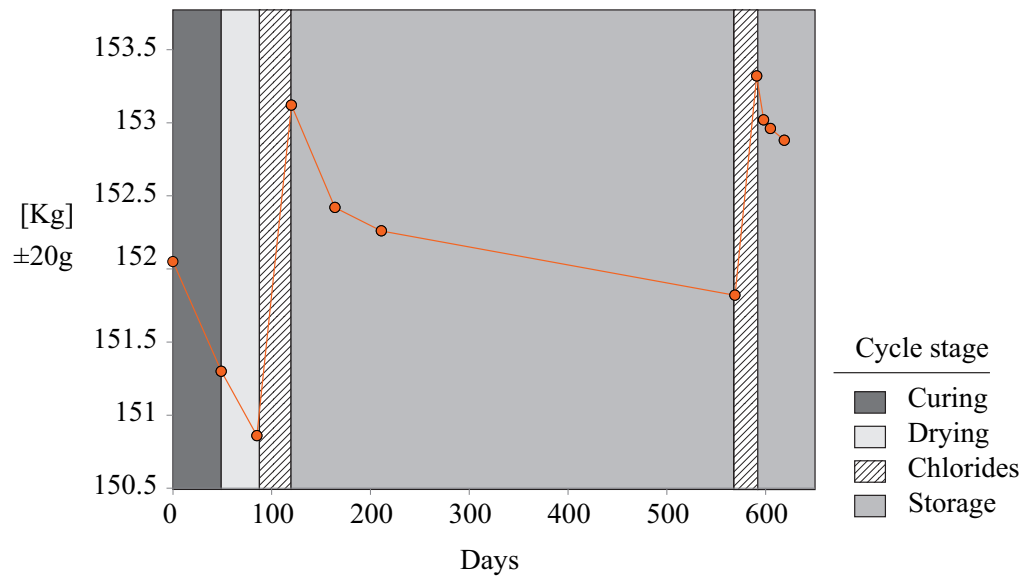
Figure 3.2: Mass evolution of specimen 1_1 during the experiment

conductivity and ±0.5 [-] for relative dielectric permittivity. From fig.3.2, it can be seen that both parameters vary in parallel with weight evolution. They decrease during evaporation phases and increase during chloride inoculations. Also it can be noted that after each cycle, although the value σ drops during evaporation, the global values increase. This confirm the expectation that after the peak due to chloride inoculation and after water has evaporated, the chloride remaining inside the concrete specimen still influences the global conductivity value; this observation was made for all specimens.

3.4 Empirical relationships

In this section, the dataset is processed with linear regressions to build an empirical relationships between chloride content, water content, relative dielectric permittivity (ε_r) and conductivity (σ). This is done, with the objective of finding a threshold value, of one or both parameters, marking out the field where reinforcement corrosion has a high probability to initiate.

3.4.1 Average ε_r and σ with respect to evaporated water

The percentage of evaporated water was calculated as follows.

* Firstly, the specimen is considered saturated with water after chloride inoculation stages. The specimen's maximum weight values corresponds to saturation.

* Secondly, the mass difference between saturation and the rest of the dataset is calculated. Dividing this difference with the mass at saturation gives the specimen mass variation in %.

Tables of results

Specimen	Saline solutions	Exposition cycle I	Exposition cycle II	Free Cl- content
1_1	165 g/l	34 days	22 days	1.75%
2_1	247.5 g/l	14 days	22 days	2.05%
2_2	165 g/l	75 days	82 days	1.60%

Table 3.1: Summary of the experiment

Specimen	Water %	dry density kg/m3
1_1	4.00	2338
2_1	4.17	2330
2_2	4.13	2351

Table 3.2: Specimen water content and dry density, all specimen present similar values, indicating that they are comparable.

Specimen	Gel pores %	Capillary pores %	Hydration pores %	Air pores %
1_1	5.4	6.3	11.6	1.9
2_1	6.0	6.0	11.9	1.7
2_2	5.4	6.2	11.6	1.4

Table 3.3: Specimen pore size distribution, showing no major difference in porosity between all specimens.

Position	Total Cl- %	Free Cl-%
Upper left	1.60	1.52
Center	1.63	1.54
Bottom right	1.51	1.45

Table 3.4: Free and total chloride content of the 5 first cm of three cores taken from specimen 1_1, presents less than 0.1% difference, only free chloride content is considered.
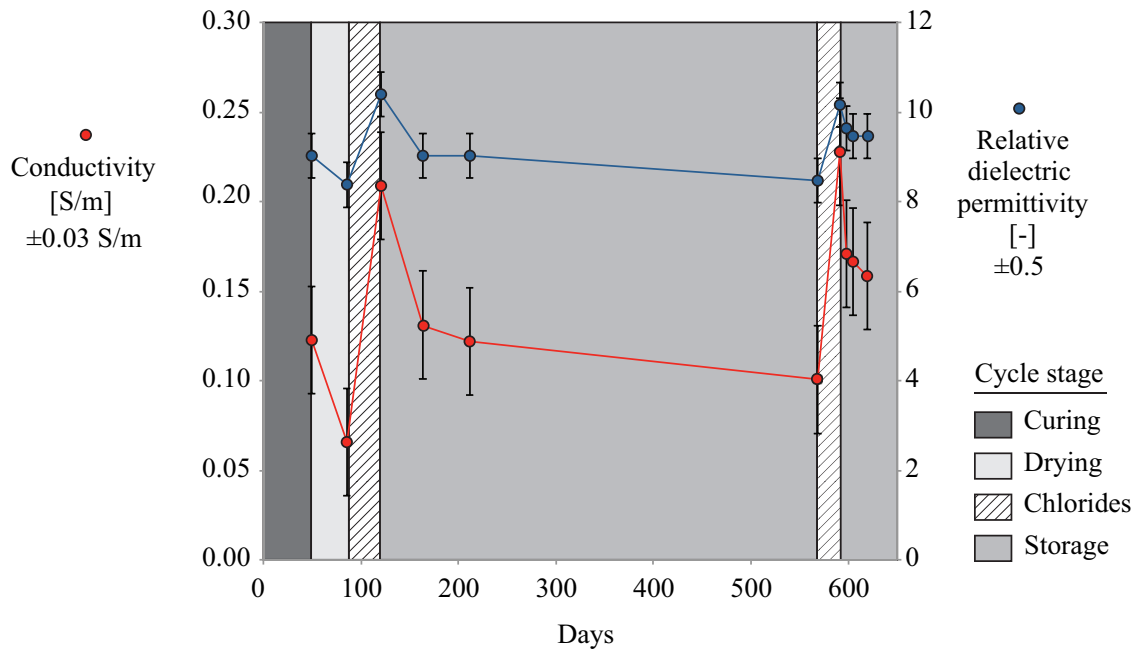
Figure 3.3: The electromagnetic parameters of specimen 1_1, evolved in parallel during the experiment. The same observation was made for specimen 2_1 and 2_2.

* Finally, knowing that evaporation affects only water molecules, the specimen mass variation is thus considered to be predominantly affected by water content.

A precision must be provided. There is a difference in the total mass of chloride between one another specimen and this may influence this dataset. However, looking at Table 3.1, one can see that the free chloride % content does not differs substantially between specimens; with a difference being of less than 0.5 percentage point.

After this, two scatter plots are constructed, linking σ and ε_r respectively calculated average values; with the corresponding mass variation %, see figure 3.4. Then a linear regression was done for both datasets and the determination coefficient R^2 was calculated. Their analysis provides the following empiric relations:

σ **and water content**   Average conductivity decreases by 0.09 S/m per 1% of evaporated water. The conductivity lower bound is 0.07 S/m when 1.8% of the specimen mass is evaporated. The parameter $\sigma = 0.20$ [S/m] at saturation, is given by the intercept of the linear regression with the maximum of specimen mass variation. The determination coefficient is 0.88, this indicates a good level of correlation, see Figure 3.4(a).

ε_r **and water content**   The average relative dielectric permittivity decreases of 1.27 per 1% of evaporated water. The permittivity lower bound is of 8 when 1.8% of the specimen mass is evaporated. And the parameter $\varepsilon_r = 10$ at saturation, is given by the intercept of the linear

regression with the maximum of specimen mass variation. The determination coefficient is of 0.66, this indicates an average level of correlation, see Figure 3.4(b).

3.4.2   Average ε_r and σ with respect to chloride content

Thereafter, two scatter plots are constructed, linking conductivity and relative dielectric permittivity, respective average values at saturation; with the corresponding chloride content. The chloride content was calculated as follows:

* The final chloride % with respect to concrete mass was obtained from destructive testing dataset, see Table 3.1. As chloride content determination requires the destruction of the specimens, this operation had to be done at the end of the experiment. As a consequence, this dataset has a limited number of data points. However, smaller control specimens were cast and exposed to the same chloride contamination procedure. Their free chloride content was measured with a water extraction procedure, at the end of the first and second cycle, see Figure 3.1(c).

* With these intermediate values provided by control specimens, it was possible to extrapolate the chloride content of the concrete specimens after first cycle. It was observed that the free chloride %, at the end of first cycle, was half the one obtained for second cycle. To extrapolate intermediate chloride % values of the concrete slabs, the respective final free chloride content of each specimen was divided by 2. Finally, the corresponding conductivity values returned form GPR measurements were assigned to these intermediate chloride content extrapolates.

* The values σ *saturation* = 0.20 S/m and ε_r *saturation* =10 [-] are given, for a water saturated specimen containing no chlorides, in figure 3.4 looking at the intercepts.

Then a linear regression was done for both datasets, and the determination coefficient R^2 was calculated. Their analysis provides the following empiric relations:
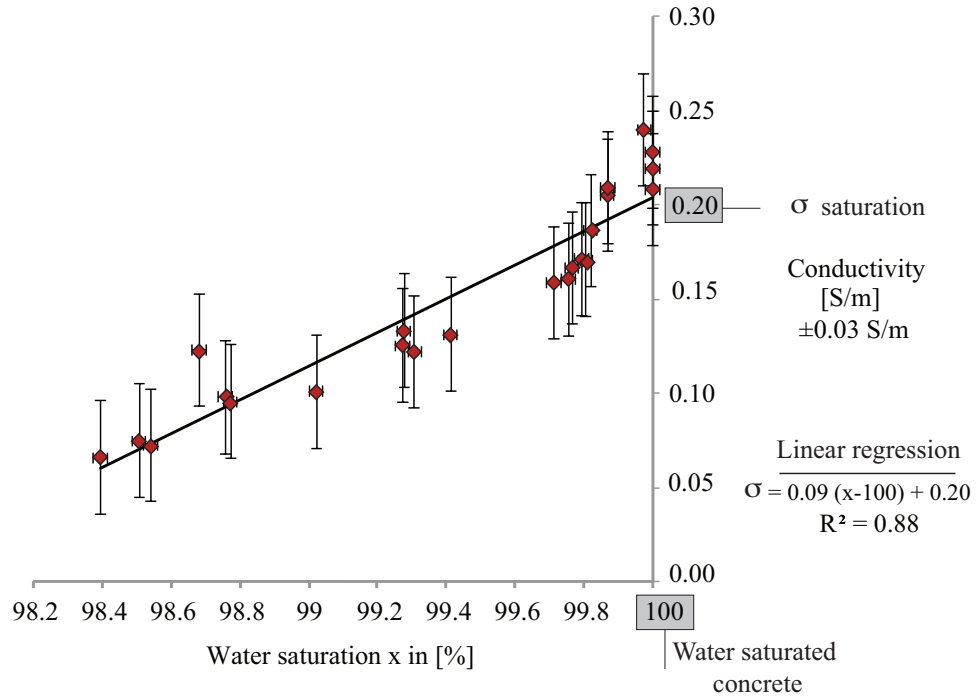
σ **at saturation and chlorides**   The relation is 0.02 [S/m] per 1% of chloride. At saturation with no chlorides conductivity, is 0.2 [S/m] and 0.25 [S/m] with 2.5% of chlorides. The determination coefficient R^2 is 0.92, this indicates a good level of correlation, see figure 3.5(a).

ε_r **at saturation and chlorides**   The determination coefficient R^2 is of 0.01, no linear relation is present between ε_r and chloride % with respect of concrete mass, see figure 3.5(b).

3.4.3   Discussion

In this experiment the variations of conductivity (σ) and relative dielectric permittivity (ε_r) were observed. These observations combined with the linear regressions showed, for this configuration, the following relation between the GPR waves EM parameters with chloride and water content: *When a Ground Penetrating Radar electromagnetic wave propagates within a concrete specimen contaminated with chlorides, the parameter σ is influenced by both water*
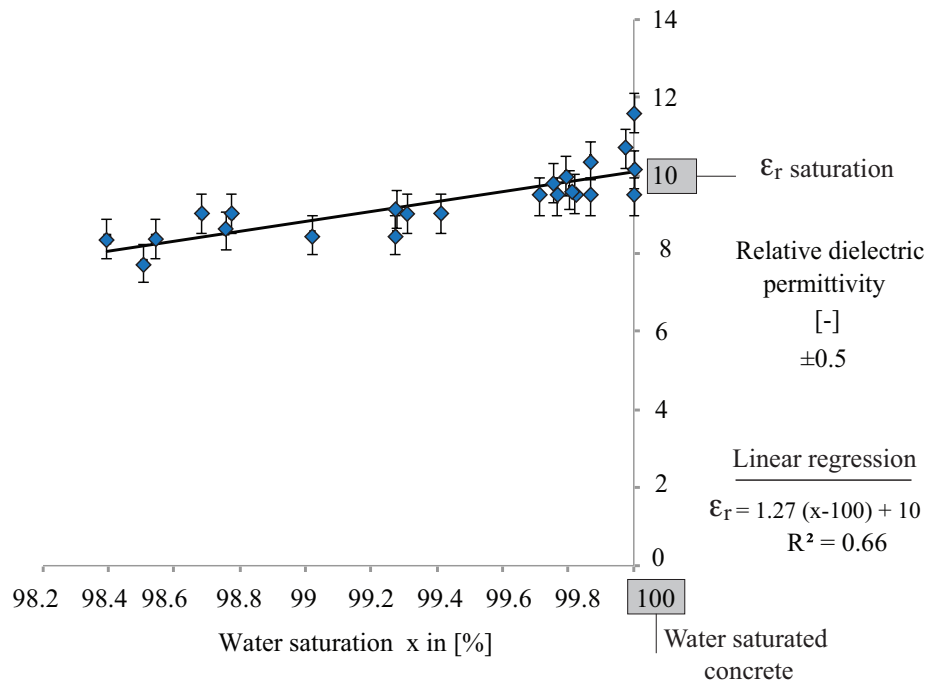
(a)

(b)

Figure 3.4: linear regression of σ and ε_r distributions with respect to specimen water saturation %

49

and chloride content, while the parameter ε_r depends, almost, only on water content. However, a relation is present between ε_r and chlorides molecules with the specimen. Because, ε_r depends on the total amount of charges that the GPR wave has encountered during its propagation inside the concrete specimen. The proportion between chloride, water and concrete influences the global ε_r of the material. This relation is expressed for different types of media, in Debye and Cole-cole models and in Topp's equation, see Rubin and Hubbard, 2005, [33]. However, complementary results indicated that all specimen were comparable with respect to concrete and water content; thus they have a similar amount of water and "concrete" charges. Only the total amount of chloride ions differs between one specimen and the other, and this difference is less than 0.5 percentage points, table 3.1. Hence, in this configuration, chloride content influences little the relative dielectric permittivity.

3.5   Conclusions

An experiment recreating chloride contamination process in concrete was designed. From it a Ground Penetrating Radar (GPR) dataset was acquired. It was expected from the experiment, to test the sensibility of GPR to chloride and moisture seasonal variation in bridge-deck-type concrete. Additionally, the possibility of finding a relationship linking concrete condition and the electromagnetic (EM) parameters calculated from the GPR dataset, was to be assessed. The average values of EM parameters were calculated from the dataset using a novel processing Time Domain Solution, described in Chapter 2. The variation of ε_r and σ in function of water and chloride content was observed. After this the dataset was processed statistically. From this study, it was found that, in this configuration, σ is influenced by water and chloride content, while ε_r is influenced, almost, only by water content. Moreover, an empirical relation using the specimen mass variation % was found. It links ε_r to water content with respect of saturation. Additionally, two other empirical relations were found, which link respectively σ to water content; σ at saturation with chloride content. Future work, will provide a solution considering a multi-layer case taking into account the presence of an asphalt layer. Also a threshold of conductivities indicating an high probability of corrosion will be investigated.
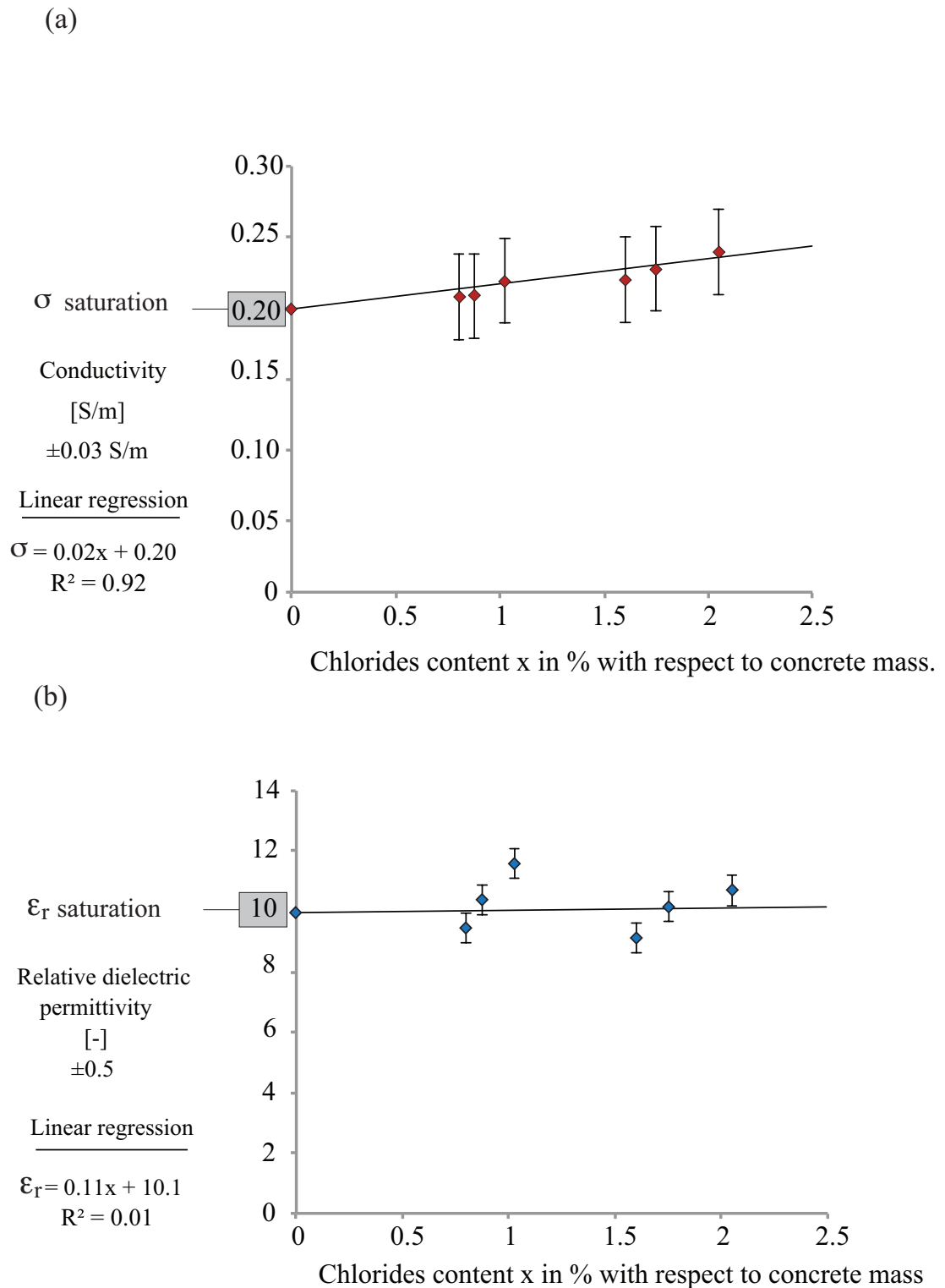
(a)

σ saturation — [0.20]

Conductivity

[S/m]

±0.03 S/m

Linear regression

σ = 0.02x + 0.20

$R^2 = 0.92$

Chlorides content x in % with respect to concrete mass.

(b)

ε_r saturation — [10]

Relative dielectric

permittivity

[-]

±0.5

Linear regression

$\varepsilon_r = 0.11x + 10.1$

$R^2 = 0.01$

Chlorides content x in % with respect to concrete mass

Figure 3.5: linear regression of σ and ε_r distributions, for concrete specimens saturated with water, with respect to chloride content

Conclusions

This doctorate thesis presented methodologies for the non-destructive determination of chloride content in concrete, for bridge decks condition monitoring, using Ground Penetrating Radar.

In Chapter 1, a novel Full-waveform inversion algorithm was developed for off-ground bistatic GPR horn antennas that uses the whole waveform of the GPR traces. The inversion enables the estimation of quantitative electromagnetic properties. The horn antenna GPR system was characterized by estimating the phase centre and the effective wavelet using measurements over a stainless-steel plate. GPR data measured over nine concrete specimens having different moisture and chloride contents were inverted and returned relative dielectric permittivity and conductivity values. The Full-waveform inversion consists of three consecutive steps. The first inversion step calibrates the time-zero using the air/concrete reflection. The second step inverts the permittivity and the frequency-dependent conductivity of the concrete using the concrete/aluminum reflection. The third step inverts the permittivity and the frequency-dependent conductivity of the concrete using both air/concrete and concrete/aluminum reflections. Third step returned similar results as in the second step. In all steps, several start models were used and returned similar results, indicating that the inversion was well constrained. In general, the inversion results showed for specimens with increasing chloride and humidity content, increasing conductivity and permittivity values, respectively, with the exception of two outliers. Chloride content presented a more accentuated effect on wave propagation than relative humidity. Finally, for increasing chloride content increasing frequency-dependent conductivity values are obtained. It was shown that it is possible to discriminate the separate effects of chloride content and relative humidity on both conductivity and relative dielectric permittivity.

In Chapter 2, a time and a frequency domain solution providing values of electromagnetic parameters for horizontally layered dielectrics were presented. Firstly, Time Domain Solution provides average values of relative dielectric permittivity $\varepsilon_r\,[-]$ and conductivity $\sigma\,[S/m]$. Secondly, an updated Full-waveform inversion, based on a novel forward model, enables the calculation of conductivity gradients for multi-layered dielectrics. The inversion considers also each reflection independently, with this provides two different informations. Top reflection inversion provides values of ε_r and σ_{top} from top concrete surface. While inverting only bottom reflection, similarly to Time Domain Solution, provides averages ε_r and σ plus a lin-

ear frequency dependent conductivity coefficient $\Delta\sigma$. Finally, the Full-waveform inversion, returns concrete slab average ε_r and conductivity gradients between top (σ_{top}) and bottom (σ_{bot}) surfaces. The methodology assessment, revealed that Time Domain Solution provides results having a reasonable accuracy, with $\pm 0.15[-]$ for ε_r and $\pm 0.01[S/m]$ for σ. Then, that the inversion procedure allows the accurate determination of conductivity gradients present within concrete. A GPR new dataset was performed with 1.2 GHz horn antennas on concrete specimens containing different chloride gradients. In parallel, the specimens were controlled with another non-destructive technique the Wenner method. At the end of the experiment, the presence of chloride gradients was controlled destructively. Thereafter, the dataset was processed with these novel methods. The GPR results are matching the ones provided from literature, a different non-destructive device and destructive testing.

In Chapter 3,   an experiment recreating chloride contamination process in concrete was designed. From it a Ground Penetrating Radar (GPR) dataset was acquired. It was expected from the experiment to test the sensibility of GPR to chloride and moisture seasonal variation in bridge-deck-type concrete. Additionally, the possibility of finding a relationship linking concrete condition and the electromagnetic (EM) parameters calculated from the GPR dataset, was to be assessed. The average values of EM parameters were calculated from the dataset using a novel processing Time Domain Solution. The variation of ε_r and σ in function of water and chloride content was observed. After this, the dataset was processed with linear regressions. From this study, it was found that in this configuration σ is influenced by water and chloride content; while ε_r is influenced, almost, only by water content. Moreover, an empirical relation using the specimen mass variation % was found. It links ε_r to water content. Additionally, two other empirical relations were found, which link respectively σ to water content ; σ at saturation with chloride content.

Future work,   will consist in, updating the Full-waveform forward model corresponding to the concrete slab's bottom reflection, using a different frequency dependent conductivity expression. Also the minimization procedure will be optimized modifying the objective function and/or using a different minimization strategy. Then a Time Domain Solution considering a multi-layer case taking into account the presence of an asphalt layer will be developed. Meanwhile, a threshold of conductivities corresponding to unsaturated concrete having a chloride content above 0.5% of cement paste will be investigated. Finally, both procedures will be applied, on real case bridge deck datasets.

Bibliography

[1] K. Arunachalam, VR Melapudi, L. Udpa, and SS Udpa. Microwave NDT of cement-based materials using far-field reflection coefficients. *NDT & E International*, 39(7):585–593, 2006.

[2] A. Benedetto and S. Pensa. Indirect diagnosis of pavement structural damages using surface GPR reflection techniques. *Journal of applied geophysics*, 62(2):107–123, 2007.

[3] H. Böhni. *Corrosion in Reinforced Concrete Structures*. Woodhead Publishing Ltd., 2005.

[4] K.J. Bois, A.D. Benally, and R. Zoughi. Microwave near-field reflection property analysis of concrete for material content determination. *Instrumentation and Measurement, IEEE Transactions on*, 49(1):49–55, 2000.

[5] KJ Bois, SD Benally, and R. Zoughi. Near-field microwave non-invasive determination of NaCl in mortar. In *Science, Measurement and Technology, IEE Proceedings-*, volume 148, pages 178–182. IET, 2001.

[6] D. Conciatori. *Effet du microclimat sur l initiation de la corrosion des aciers d armature dans les ouvrages en beton arme*. PhD thesis, Ecole Polytechnique Fale de Lausanne, 2005.

[7] L. Crocco and F. Soldovieri. Prospecting in a layered medium via microwave tomography. *Annals of Geophysics*, 46:559–572, 2003.

[8] X. Derobert, J. Iaquinta, G. Klysz, and J. P. Balayssac. Use of capacitive and GPR techniques for the non-destructive evaluation of cover concrete. *NDT & E International*, 41:44–52, 2008.

[9] B. Elsener. Half-cell potential mapping to assess repair work on RC structures. *Construction and Building Materials*, 15(2-3):133–139, 2001.

[10] B. Elsener, L. Zimmermann, and H. Böhni. Non destructive determination of the free chloride content in cement based materials. *Materials and Corrosion*, 54(6):440–446, 2003.

[11] J.R. Ernst, A.G. Green, H. Maurer, and K. Holliger. Full-waveform inversion of cross-hole radar data based on 2-d finite difference time domain solutions of maxwell s equations. *IEEE Transactions on Geoscience and Remote Sensing*, 45:2807–2828, 2007.

[12] P. Gu and JJ Beaudoin. Dielectric behavior of hardened cement paste systems. *Journal of materials science letters*, 15(2):182–184, 1996.

[13] R.H. Haddad and I.L. Al-Qadi. Characterization of portland cement concrete using electromagnetic waves over the microwave frequencies. *Cement and concrete research*, 28(10):1379–1391, 1998.

[14] U.C. Hasar. Non-destructive testing of hardened cement specimens at microwave frequencies using a simple free-space method. *NDT & E International*, 42:550–557, 2009.

[15] J. Hugenschmidt and R. Loser. Detection of chlorides and moisture in concrete structures with ground penetrating radar. *Materials and Structures*, 41:785–792, 2007.

[16] J. Hugenschmidt and R. Mastrangelo. GPR inspection of concrete bridges. *Cement and Concrete Composites*, 28:384–392, 2006.

[17] K.Z. Jadoon, E. Slob, M. Vanclooster, H. Vereecken, and S. Lambot. Uniqueness and stability analysis of hydrogeophysical inversion for time-lapse ground-penetrating radar estimates of shallow soil hydraulic properties. *Water Resour. Res*, 44:W09421, 2008.

[18] A. Kalogeropoulos, J. van der Kruk, J. Hugenschmidt, K. Merz, and S. Busch. Chlorides and moisture assessment in concrete by GPR full waveform inversion. *Near Surface Geophysics*, 9:277–285, 2011.

[19] W. Kim, A. Ismail, NL Anderson, EA Atekwana, and A. Buccellato. Non-destructive testing (NDT) for corrosion in bridge decks using GPR. In *3rd International Conference on Applied Geophysics, Hotel Royal Plaza, Orlando, Fla*, 2003.

[20] A. Klotzsche, J. van der Kruk, G.A. Meles, J. Doetsch, H. Maurer, and N. Linde. Full-waveform inversion of cross-hole ground-penetrating radar data to characterize a gravel aquifer close to the thur river, switzerland. *Near Surface Geophysics*, 8:635–649, 2010.

[21] G. Klysz and J.P. Balayssac. Determination of volumetric water content of concrete using ground-penetrating radar. *Cement and Concrete Research*, 37(8):1164–1171, 2007.

[22] G. Klysz, JP Balayssac, and X. Ferrières. Evaluation of dielectric properties of concrete by a numerical FDTD model of a GPR coupled antenna–parametric study. *NDT & E International*, 41(8):621–631, 2008.

[23] G. Klysz, J.P. Balayssac, and S. Laurens. Spectral analysis of radar surface waves for non-destructive evaluation of cover concrete. *NDT & E International*, 37(3):221–227, 2004.

[24] C. Kohl and D. Streicher. Results of reconstructed and fused NDT-data measured in the laboratory and on-site at bridges. *Cement and Concrete Composites*, 28(4):402–413, 2006.

[25] J.C. Lagarias, J. A. Reeds, M. H. Wright, and P. E. Wright. Convergence properties of the nelder-mead simplex method in low dimensions. *Society for Industrial and Applied Mathematics*, 9:112–147, 1998.

[26] WL Lai, T. Kind, and H. Wiggenhauser. Frequency-dependent dispersion of high-frequency ground penetrating radar wave in concrete. *NDT & E International*, 2011.

[27] WL Lai, SC Kou, WF Tsang, and CS Poon. Characterization of concrete properties from dielectric properties using ground penetrating radar. *Cement and Concrete Research*, 39(8):687–695, 2009.

[28] S. Lambot, E.C. Slob, I. Vandenbosch, B. Stockbroeckx, and M. Vanclooster. Modeling of ground-penetrating radar for accurate characterization of subsurface electric properties. *IEEE Transactions on Geoscience and Remote Sensing*, 42:2555–2568, 2004.

[29] S. Laurens, JP Balayssac, J. Rhazi, G. Klysz, and G. Arliguie. Non-destructive evaluation of concrete moisture by GPR: experimental study and direct modeling. *Materials and structures*, 38(9):827–832, 2005.

[30] A.G. Meles, J. van der Kruk, S. Greenhalgh, J. Ernst, H. Maurer, and A.G. Green. A new vector waveform inversion algorithm for simultaneous updating of conductivity and permittivity parameters from combination crosshole-/borehole-to-surface gpr data. *IEEE Geoscience and Remote Sensing*, 48:3391–3407, 2010.

[31] G. Miller, P. Gaydecki, S. Quek, B. Fernandes, and M. Zaid. A combined q and heterodyne sensor incorporating real-time DSP for reinforcement imaging, corrosion detection and material characterisation. *Sensors and Actuators A: Physical*, 121(2):339–346, 2005.

[32] A. Robert. Dielectric permittivity of concrete between 50 MHz and 1 GHz and gpr measurements for building materials evaluation. *Journal of Applied Geophysics*, 40:89–94, 1998.

[33] Y. Rubin and S.S. Hubbard. *Hydrogeophysics*, volume 50. Springer Verlag, 2005.

[34] Z.M. Sbartai, S. Laurens, J.P. Balayssac, G. Ballivy, and G. Arliguie. Effect of concrete moisture on radar signal amplitude. *ACI materials journal*, 103(6), 2006.

[35] Z.M. Sbartaï, S. Laurens, J.-P. Balayssac, G. Arliguie, and G. Ballivy. Ability of the direct wave of radar ground-coupled antenna for NDT of concrete structures. *NDT E International*, 39(5):400 – 407, 2006.

[36] M. Scott, A. Rezaizadeh, A. Delahaza, CG Santos, M. Moore, B. Graybeal, and G. Washer. A comparison of nondestructive evaluation methods for bridge deck assessment. *NDT & E International*, 36(4):245–255, 2003.

[37] M. N. Soutsos, J. H. Bungey, S. G. Millard, M. R. Shaw, and A. Patterson. Dielectric properties of concrete and their influence on radar testing. *NDT&E International*, 34:419–425, 2001.

Bibliography

[38] R. Streich and J. van der Kruk. Characterizing a GPR antenna system by near-field electric field measurements. *Geophysics*, 72(5):A51, 2007.

[39] J. van der Kruk, R. Streich, and A. G. Green. Properties of surface waveguides derived from separate and joint inversion of dispersive TE and TM GPR data. *Geophysics*, 71:K19–K29, 2006.

[40] G. Villain, X. Derobert, O. Abraham, O. Coffec, O. Durand, L. Laguerre, and Baltazart. Use of ultrasonic and electromagnetic NDT to evaluate durability monitoring parameters of concrete. In *NDTCE09 proceedings*, 2009.

A I - Laws of electromagnetism

Laws of electromagnetism with Newton's laws are the socle of classical physics, they describe what matter is, how it moves and interacts. This appendix is dedicated to the description of the laws constituting the physics of electromagnetic waves propagation. The laws are introduced in the case of a source in vacuum and then are developed within dielectrics. As a preamble to these laws two principles and one force must be introduced.

...

The charge conservation principle describes the evolution of a charge across time, in Eq. A.1. This principle enunciates that the amount of current J flowing outward an hypothetical closed surface is opposite to the amount by which the charge density ρ is decreasing per time unit.This maps the fact that a charge does not disappear into (or is created out of) nothingness, it decreases in a region of space only because it flows into other regions.

$$\nabla \cdot J = -\frac{\partial \rho}{\partial t} \tag{A.1}$$

Superposition principle In physics of electromagnetism the superposition principle states that the total electric field E generated by two or more electromagnetic waves is the sum of each individual electric field E_1 and E_2. This principle implies that a wave can be decomposed in a sum of waves interacting one with another by addition or subtraction.

$$E = E_1 + E_2 \tag{A.2}$$

Lorentz force The resulting force applied on a charge q in motion with a velocity v by electromagnetic fields, with E the electric field and B the magnetic flux density, is called the Lorentz force. It justifies how, to exist, a magnetic force requires a charge displacement. While an electric force, similar to gravity, exists at the moment that a charge is present. Lorentz force F is given by:

$$F = q(E + v \times B) \tag{A.3}$$

Maxwell's Law

In 1865, James Clerk Maxwell modified and unified a set of laws describing electrostatic and magnetostatic phenomenas. By doing so, he gave rise to "A Dynamical Theory of the Electromagnetic Field", describing all classical electromagnetic phenomena. *Maxwell's laws* are composed of four equation expressed in vacuum as follows:

Gauss's Law   expresses the electric fluxes D through a closed surface of an hypothetical volume depending on its charge density ρ.

$$\nabla \cdot D = \rho \tag{A.4}$$

Gauss's law for magnetism   states that the magnetic flux B coming out of any hypothetical closed surface is null, implying this way that there is no magnetic equivalent to electric charges.

$$\nabla \cdot B = 0 \tag{A.5}$$

These first two laws are static, they describe the electromagnetic fields intensities using $\nabla \cdot$ operator. The third and fourth law, *Faraday's law of induction* Eq. A.6 and the *corrected Ampere's law* Eq. A.7, use $\nabla \times$ operators, this introduces the notion of circulation within the fields.

Faraday's law of induction   defines that a circulation in E, the electric field, generates a flux of B, the magnetic flux density. The flux of B is perpendicular to the plane of circulation and depends of its orientation.

$$\nabla \times E = -\frac{\partial B}{\partial t} \tag{A.6}$$

Corrected Ampere's law   shows that a circulation in H the magnetic field, induces a flux of D, the electric displacement that is also perpendicular to the plane of circulation, also it depends on its orientation.

$$\nabla \times H = J + \frac{\partial D}{\partial t} \tag{A.7}$$

In Eq. A.4 and A.7 the parameters ρ, J are the charge and the current densities of any external charge, they are the sources of the electromagnetic fields. For field propagation problems these densities are localized in space, for instance, in the case of Ground Penetrating Radar they are restricted to flow in an antenna. The displacement current term $\partial D/\partial t$ (added by Maxwell) in Eq. A.7 predicts the existence of propagating electromagnetic fields. When a charge density ρ is moving creating that way a current density J . The generated electric and magnetic fields are radiated away from the source and propagate using alternatively $\nabla \times H = \partial D/\partial t$ and $\nabla \times E = -\partial B/\partial t$ the *source free* terms of Ampere's and Faraday's law. This explains how light (more generally all electromagnetic waves), at the opposite of sound, travel through matter-free spaces.

Constitutive relations

Vacuum The electric and magnetic flux densities D $[C/m^2]$, B $[T]$ are interrelated to the field intensities E $[V/m]$ and H $[A/m]$ in vacuum with the following *constitutive relations*:

$$D = \varepsilon_0 E \tag{A.8}$$

$$B = \mu_0 H \tag{A.9}$$

with ε_0 the *vacuum permittivity* having for numerical value 8.854×10^{-12} [F/m]. And μ_0 the *vacuum permeability* having for numerical value $4\pi \times 10^{-7}$ [H/m]. From these two quantities, two other physical constants are defined c_0 the *speed of light in vacuum* and η_0 the *characteristic impedance of vacuum*.

$$c_0 = \frac{1}{\sqrt{\mu_0 \varepsilon_0}} = 3 \times 10^8 \, [m/s] \tag{A.10}$$

$$\eta_0 = \sqrt{\frac{\mu_0}{\varepsilon_0}} = 377 \, [\Omega] \tag{A.11}$$

Matter In the case of matter the simplest expression of this relations is for an homogeneous isotropic lossless dielectric and magnetic material:

$$D = \varepsilon E \tag{A.12}$$

$$B = \mu H \tag{A.13}$$

ε and μ being the *dielectric permittivity* and the *magnetic permeability* of the material. They are related to the *electric* (χ) *and magnetic* (χ_m) *susceptibilities* accounting for the polarization properties of the material as such:

$$\varepsilon = \varepsilon_0 (1 + \chi) \tag{A.14}$$

$$\mu = \mu_0 (1 + \chi_m) \tag{A.15}$$

Equations A.14 and A.15 can be rewritten under the form:

$$\varepsilon_r = \frac{\varepsilon}{\varepsilon_0} = 1 + \chi \tag{A.16}$$

$$\mu_r = \frac{\mu}{\mu_0} = 1 + \chi_m \tag{A.17}$$

giving rise that way to the *relative dielectric permittivity* ε_r and to the *relative magnetic permeability* μ_r. With this c the *speed of propagation of the electromagnetic fields in the material* and η the *impedance of the material* can be expressed likewise:

$$c = \frac{c_0}{\sqrt{\varepsilon_r \mu_r}} \tag{A.18}$$

$$\eta = \eta_0 \sqrt{\frac{\mu_r}{\varepsilon_r}} \tag{A.19}$$

in this PhD the electromagnetic properties of non-magnetic materials will be investigated. In such cases $\mu = \mu_0$ thus $\mu_r = \mu/\mu_0 = 1$. Consequently c and η only depend on ε_r the relative dielectric permittivity of the material.
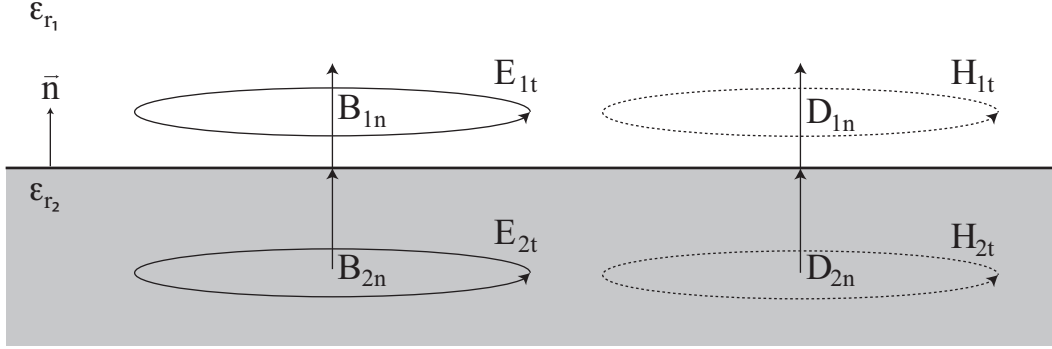
Figure A.1: Boundary conditions; the tangential components of the electric E_t and magnetic H_t *fields* are continuous across the boundary, and the normal components of the electric D_n and magnetic B_n *fluxes densities* are continuous across the boundary

Boundary conditions

The exchange of energy between two materials is given by the *boundary conditions*. In the general case each interface is seen as a potential source. The boundary condition for the electromagnetic fields across two materials is given by:

$$E_{1t} - E_{2t} = 0 \tag{A.20}$$

$$H_{1t} - H_{2t} = J_S \times \vec{n} \tag{A.21}$$

$$D_{1n} - D_{2n} = \rho_s \tag{A.22}$$

$$B_{1n} - B_{2n} = 0 \tag{A.23}$$

where $\vec{n}$ is a unit vector normal to the boundary pointing from medium 2 towards medium 1. E_t and H_t are the tangential components of the electric and magnetic fields. D_n and B_n are the normal components of the electric and magnetic flux densities. The quantities ρ_s and J_s are any external surface charge and surface current densities on the boundary surface. In the case studied in this PhD there were no externally applied surface charges nor currents at the material boundaries, which allows stating the following *source-free boundary conditions*:

$$E_{1t} = E_{2t} \tag{A.24}$$

$$H_{1t} = H_{2t} \tag{A.25}$$

$$D_{1n} = D_{2n} \tag{A.26}$$

$$B_{1n} = B_{2n} \tag{A.27}$$

In words, the tangential components of the electric E_t and magnetic H_t fields are continuous across the boundary, and the normal components of the electric D_n and magnetic B_n fluxes densities are continuous across the boundary, Fig.A.1.

Electromagnetic waves

Harmonic time dependence   Due to their alternation the electromagnetic fields can be considered having harmonic time dependence. This allows considering the propagating fields as plane waves and using a sinusoidal representation to describe them. A plane wave is an ideal wave whom wavefronts are parallel with one another, see Figure A.2. This PhD considers time dependent electromagnetic fields in the form of propagating plane waves.

Sinusoidal wave   A convenient way to represent a plane wave is to consider it as a sine function of time. It can be expressed under the following form:

$$y(t) = A \sin(kx - \omega t + \varphi) + D \tag{A.28}$$

with:

A the *amplitude* $[V]$[1]
t the *time* $[s]$
x the *position* $[m]$
φ the *phase* $[rad]$
k the *wavenumber* $[rad/m]$
ω the *angular frequency* $[rad/s]$
D the *DC offset* for a non-null center amplitude $[V]$

relations:

$k = 2\pi/\lambda = 2\pi f/c$, with λ the *wavelength* $[m]$ and f the *frequency* $[Hz]$.

$\omega = 2\pi/T = 2\pi f$, with T the *period* $[s]$ and f the *frequency* $[Hz]$.

also $k = \omega/c$ and $c = \lambda f$.

Phasors   Using *Euler's formula* a sine wave takes the following complex phasor representation, with $j^2 = -1$:

$$y(t) = A \cdot sin(\omega t + \varphi) = \frac{A}{2} e^{j(\omega t + \varphi)} - \frac{A}{2} e^{-j(\omega t + \varphi)} \tag{A.29}$$

with $y(t) = \Re[Ae^{j(\omega t + \varphi)}] = \Re[Ae^{j\varphi} \cdot e^{j\omega t}]$.

---

[1]In the case of GPR, electromagnetic waves are recorded measuring the amount of J currents $[Am^{-2}]$ flowing in the antenna having a conductivity σ $[Sm^{-1}] = [AVm^{-1}]$. Following Ohm's law $E = J/\sigma = [Am^{-2}]/[AV^{-1}m^{-1}] = [Vm^{-1}]$. The antenna having a finite size [m], the amplitude of the currents flowing in the antenna is expressed in [V].
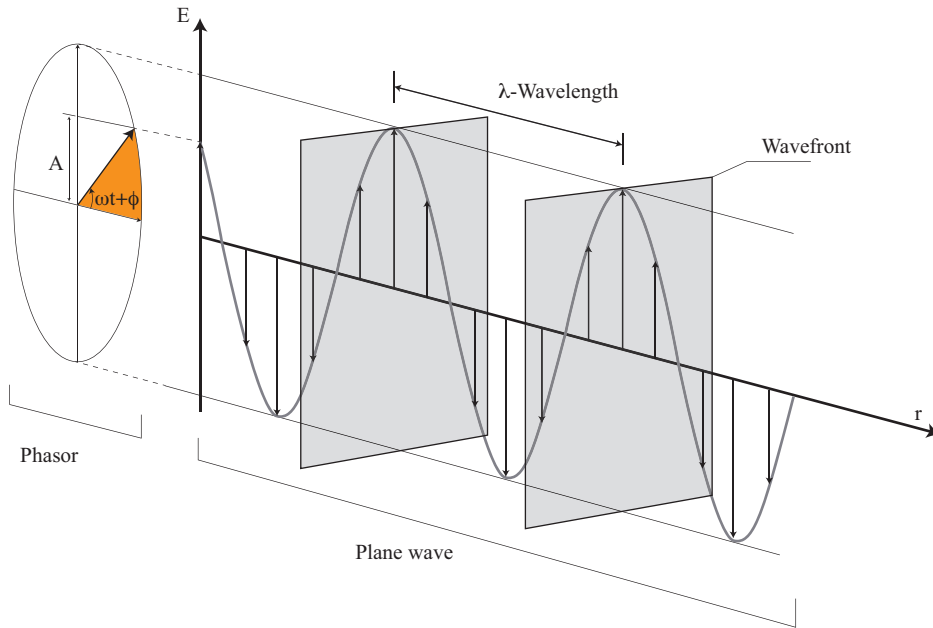
Figure A.2: A sinusoidal plane wave and it's phasor representation in the electric field *E* propagating in the *r* direction.

Fourier transform   A wave propagating in an *r* direction can be represented in the *Frequency domain* using the *Fourier transform* and its reciprocal the *inverse Fourier transform*

$$\hat{y}(r,\omega) = \int_{-\infty}^{+\infty} y(r,t) e^{-j\omega t} dt \tag{A.30}$$

$$y(r,t) = \frac{1}{2\pi} \int_{-\infty}^{+\infty} \hat{y}(r,\omega) e^{j\omega t} d\omega \tag{A.31}$$

The notation $\hat{y}$ is used to represent frequency domain, while the notation y stands for time domain.

Time harmonic form of Maxwell's equations   Assuming that all fields have a time dependence $j\omega t$, and replacing the time derivatives by the phasor representation $\partial/\partial t \rightarrow j\omega$ Maxwell's equations can be rewritten under the form:

$$\nabla \cdot D = \rho \tag{A.32}$$

$$\nabla \cdot B = 0 \tag{A.33}$$

$$\nabla \times E = -j\omega B \tag{A.34}$$

$$\nabla \times H = J + j\omega D \tag{A.35}$$
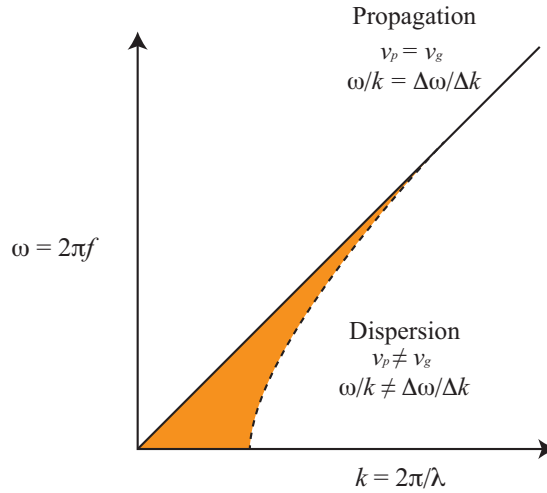
Figure A.3: Dispersion relation

Lossy dielectric materials

All real materials are in fact lossy, losses are expressed in Amperes law eq. A.35. The law states that any real dielectric medium subjected to an electric displacement field D will react moving the charges constituting it generating a current density J. In a dielectric material, two types of charges movement must be differentiated: the *bounded charges* characterized by polarization/displacement current density J_d and the *free charges* that are characterized by *conduction current density* J_c. Theses current densities are related to the total current density J as follows:

$$J = J_c + J_d \tag{A.36}$$

Relative dielectric permittivity   Under the influence of an electric field, the movement of *bound charges* in a medium is defined with the *relative dielectric permittivity* ε_r [-], that is related to the polarization properties of the material, see A.14, which gives up to polarization direction:

$$J_d = \varepsilon_r \frac{\partial E}{\partial t} \tag{A.37}$$

In lossy dielectrics when a electromagnetic wave propagates, the dielectric bound charges polarization response time will differ depending on the frequency of the solicitation. This as for effect that some electromagnetic waves will propagate in a slower fashion with respect to others. This delays the phase of some harmonic sine functions forming the pulse.

Dispersion   Pulses can also be described with harmonic time dependent sine functions, using superposition principle. A pulse will propagate in space with a group velocity v_g, and it is described by a set of harmonic sine waves having each one a phase velocity v_p. These parameters depend on the pulsation ω and the wave number k of the pulse as follows:

$$v_p = \frac{\omega}{k} \tag{A.38}$$

$$v_g = \frac{\Delta\omega}{\Delta k} \tag{A.39}$$

Dispersion occurs when,

$$v_p \neq v_g \Leftrightarrow \frac{\omega}{k} \neq \frac{\Delta\omega}{\Delta k} \tag{A.40}$$

The group velocity of a electromagnetic pulse is given by:

$$v_g = \frac{c_0}{\sqrt{\varepsilon_r}} \tag{A.41}$$

And the phase velocity v_p of one harmonic sine function is defined with:

$$v_p = \frac{c_0}{\sqrt{\varepsilon_r(1 - \frac{\sigma}{\omega\varepsilon_r})}} \tag{A.42}$$

From these relations and from the dispersion relation presented in figure A.3 the following is observed:

* If $\sigma/\omega\varepsilon \gg 1$ then $\omega/k \neq \Delta\omega/\Delta k$ the pulse has a dispersive behavior, harmonic sine functions will interfere.

* If $\sigma/\omega\varepsilon \ll 1$ then $\omega/k \simeq \Delta\omega/\Delta k$ the pulse has a propagative behavior, harmonic sine functions are in phase.

The transition frequency of a material can be calculated with the loss tangent $\tan\delta$ that it is usual to define as :

$$\tan\delta = \frac{\sigma}{\omega\varepsilon_r} \tag{A.43}$$

Then the transition between propagation and dispersion is when $\tan\delta = 1$ hence

$$\frac{\sigma}{2\pi f\varepsilon} = 1. \tag{A.44}$$

The transition frequency is then,

$$f_t = \frac{\sigma}{2\pi\varepsilon_r\varepsilon_0}. \tag{A.45}$$

Below that frequency, for a given value of ε_r and σ, the waves have a dispersive behavior, pulse is spreading, $\sigma/\omega\varepsilon \gg 1$. Above that frequency, for a given value of ε_r and σ, the waves have a propagative behavior, pulse shape is preserved, $\sigma/\omega\varepsilon \ll 1$. See figure A.4. This Phd used an 1.2 [GHz] GPR antenna, a conservative transition frequency $f_t = 450$ [MHz] can be calculated for this study with $\varepsilon_r = 10$ [-] and $\sigma = 0.25$ [S/m] with equation A.45. Full-waveform inversion is done in this frequency range, from 800 [MHz] to 2.85 [GHz], and Time Domain Solution returns values for the centre frequency of the GPR pulse. Hence in this study the relative dielectric permittivity parameter is frequency independent.
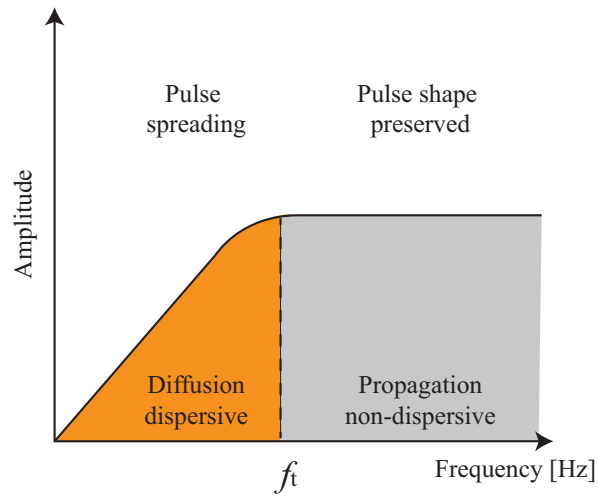
Figure A.4: Wave behavior below and above transition frequency

Electric conductivity Under the influence of an electric field, the displacement of *free charges* in a medium is defined with the *electric conductivity* σ [S/m] expressed with Ohm's law as such:

$$j_c = \sigma E \tag{A.46}$$

In lossy materials, free charges will not require the same amount of energy for their displacement. Phenomenologically this loss is due to collision between particles in material's atomic structure (electric friction). In this PhD, Time Domain Solution does not take into account this effect. Reversely Full-waveform inversion considered $\Delta\sigma$ the linear loss in amplitudes for each harmonic sine expressed with:

$$\sigma(f, \sigma_{f_c}, \Delta\sigma) = \sigma_{f_c} + \frac{f - f_c}{f_c} \Delta\sigma. \tag{A.47}$$

A | II - Time domain solution simplifications

Introduction

Time Domain Solution can be used to estimate the relative dielectric permittivity ε_r and conductivity σ of an object. It is based on the resolution of a direct problem and requires the geometry of the object to be known. The method uses the relative difference in time and amplitude of electromagnetic waves reflections. It requires the prior knowledge of the distance between reflectors. The analysis is based on the identification of the maximum of each reflection, the positive peaks. Each peak is defined by a time and an amplitude value, see chapter 2.

Simplifying hypothesis

The methodology is based on several simplifications. First only the center frequency is considered, i.e. 1.2 [GHz].

The bi-static system is considered as monostatic The traveled distance inside the concrete specimen is assumed being equal to the slab thickness. This implies that θ_2 the angle of transmission, Fig.A.1 is equal to 0. This implies the velocity to be underestimated, because the considered distance is less important that the one really crossed. The monostatic hypothesis requires to consider the reflections inside the concrete specimen to be perpendicular to the concrete slab surface $\theta_2 = 0$, and θ_1' to be considered as equal to θ_1.

Slab homogeneity Because the methodology compares one reflection with another, the object has to be considered homogeneous. The dielectric permittivity ε_r and conductivity σ are assumed to be the same in every part of the object.

Medium properties At the centre frequency of the antennas, the pulse experiences a propagative regime, ε_r is frequency independent. Meanwhile the frequency dependence of σ expressed in the Full-waveform inversion using $\Delta\sigma$ is not taken into account in Time Domain Solution. Conductivity is assumed to be frequency independent, see appendix I.
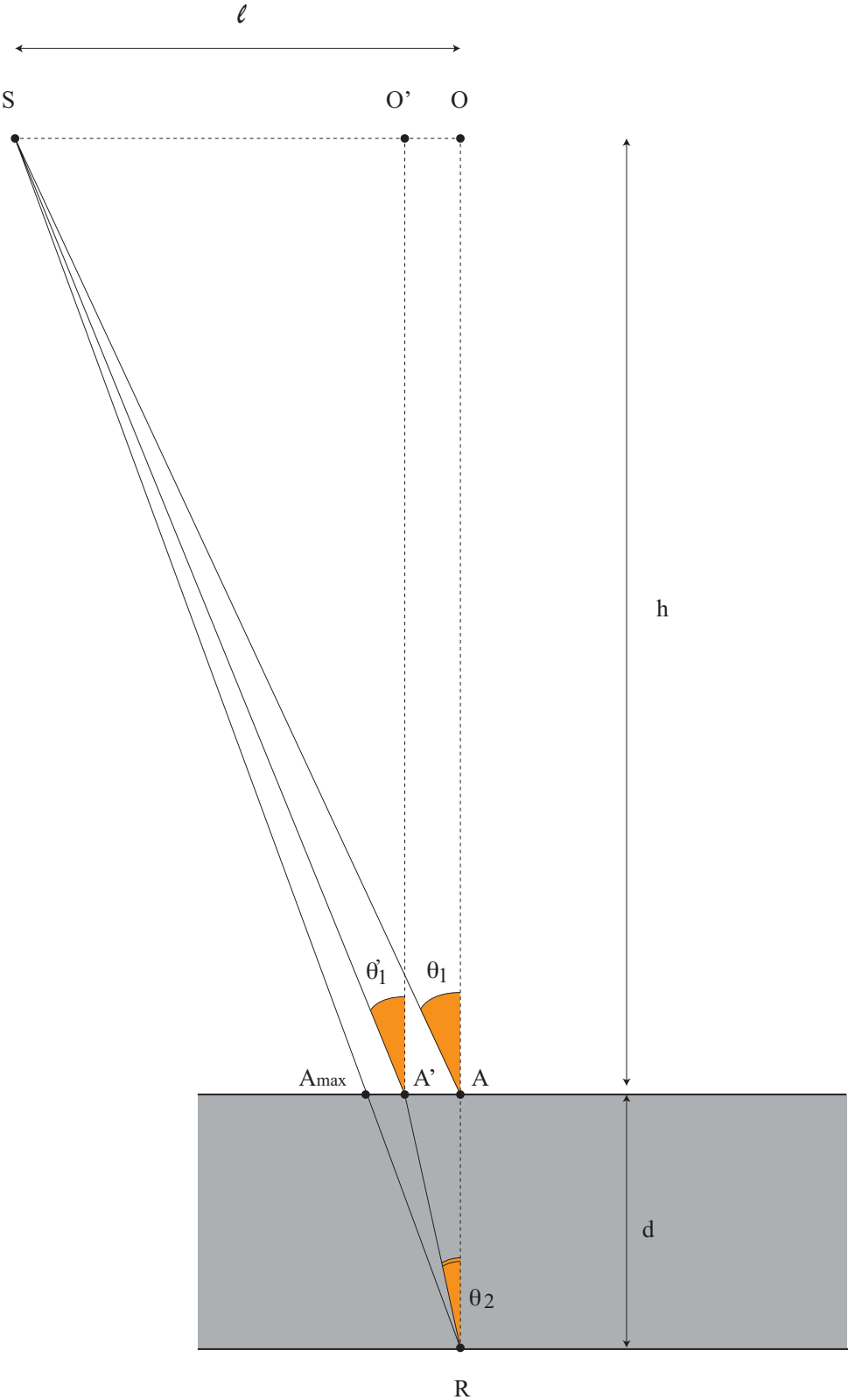
Figure A.1: Geometry of the problem

Induced error

In this section, it is proposed to estimate the error induced with the hypothesis of a pulse reflection perpendicular at an interface. The monostatic hypothesis considers that θ_2 the angle of the transmitted signal equal to 0. This has for consequence that the travelled distance is underestimated, thus the velocity is underestimated and the returned dielectric permittivity ε_r is overestimated. Considering now, $\theta_2 \neq 0$,what is the real travelled distance ? What is the error induced on the returned dielectric permittivity ε_r?

Snell-Descartes law provides the following identities :

$$\frac{sin\theta_1}{sin\theta_2} = \frac{v_1}{v_2} = \frac{n_2}{n_1}. \tag{A.1}$$

The angles of reflection θ_1' and transmission θ_2, are dependent of the velocities ratio v_1/v_2; it is thus not possible to determine directly angles values. In Fig.A.1 the problem is presented. The peak to peak methodology considers the real path A'R, equal to an hypothetical path AR, for the same time of propagation Δt. Using the previous relations we now that:

$$v_{AR} = \frac{AR}{\Delta t} = \frac{c_0}{\sqrt{\varepsilon_{r_{AR}}}} \iff \Delta t = \frac{\sqrt{\varepsilon_{r_{AR}}}}{c_0} AR \tag{A.2}$$

and

$$v_{A'R} = \frac{A'R}{\Delta t} = \frac{c_0}{\sqrt{\varepsilon_{r_{A'R}}}} \iff \Delta t = \frac{\sqrt{\varepsilon_{r_{A'R}}}}{c_0} A'R \tag{A.3}$$

we then find that

$$\frac{AR}{A'R} = \frac{\sqrt{\varepsilon_{r_{A'R}}}}{\sqrt{\varepsilon_{r_{AR}}}} = cos\theta_2 \tag{A.4}$$

Thus the approximation is of $cos\theta_2$ and the induced error on ε_{r_2} is equal to $\varepsilon_{error} = 1 - (cos\theta_2)^2$. But as mentioned before it is not possible to determine the exact value of $cos\theta_2$ because it depends of the estimation of v_2 and consequently of ε_{r_2}, v_1 being fixed.

It is proposed now to calculate what would be the maximum induced error. This worst case is represented by the point A_{max} there the following relation is present $\theta_1' = \theta_2$ thus $v_1 = v_2$ and $\varepsilon_{r_1} = \varepsilon_{r_2}$. In this hypothetical situation, where a reflection should not occur, the value of θ_2 is given by :

$$tan\theta_2 = \frac{l}{h+d} = \frac{SO}{OR} \tag{A.5}$$

because A_{max} is on SR. In this case $h + d = 38$ [cm] and $l = 14$ and $\theta_2 = 20.22$. Then using Eq. (A.4) we find that :

$$\frac{\sqrt{\varepsilon_{r_{A'R}}}}{cos\theta_2} = \sqrt{\varepsilon_{r_{AR}}}.$$

It is now proposed to estimate the error induced in the calculation of ε_r

Worst case

In this specific case $\varepsilon_{r_1} = \varepsilon_{r_2} = 1$, the estimated dielectric permittivity using Time Domain Solution methodology will be of :

$$\varepsilon_{r_{AR}} = \left(\frac{1}{cos\theta_2}\right)^2 = \left(\frac{1}{cos(20.22)}\right)^2 = 1.136$$

The maximum error induced on the determination of the dielectric permittivity is of

$$\varepsilon_{error} = 1 - (cos\theta_2)^2 = 1 - (cos20.22)^2 = 0.12$$

In this case because of the geometrical configuration of the test set-up defined by h, d and l, the maximum error on the relative dielectric permittivity is 12%.

Case using concrete permittivity

The minimum value of dielectric permittivity provided in literature for dry concretes is $\varepsilon_{r_2} = 4[-]$. Using Snell-Descartes law and using the worst case value of $\theta_1' = 20.22$, we have:

$$\frac{sin\theta_1}{sin\theta_2} = \frac{v_1}{v_2} = \frac{\sqrt{\varepsilon_{r_2}}}{\sqrt{\varepsilon_{r_1}}},$$

with this

$$sin\theta_2 = \frac{\sqrt{\varepsilon_{r_1}}}{\sqrt{\varepsilon_{r_2}}} sin\theta_1 = \frac{1}{\sqrt{4}} sin(20.22) \Longleftrightarrow \theta_2 = 9.95$$

The error on the estimated permittivity would be then of $\varepsilon_{error} = 1 - (cos\theta_2)^2 = 0.03$, This means that the error induced by this simplification, using Time Domain Solution, on values of relative dielectric permittivity is of maximum 3%.

A   III - Chloride transportation processes

This section proposes a brief picture of chloride and water transportation processes within concrete pores.

* During curing stage, water within the pores evaporates and is absorbed by cement hydration, see figure A.1 and A.2.

* During chloride contamination, the saline solution migrates through the pores of concrete, figure A.3. The specimen is saturated with water.

* After chloride contamination, water evaporates without mobilizing chlorides. The ions remain inside concrete and migrate with diffusion processes, figure A.4.

* A new cycle begins.

As a consequence of these transportation processes it is expected for chloride ions, to be distributed in gradients, within a concrete structure, see Conciatori, 2005, [6].

Initial state
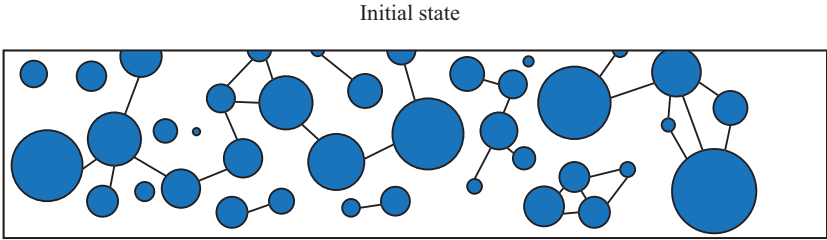
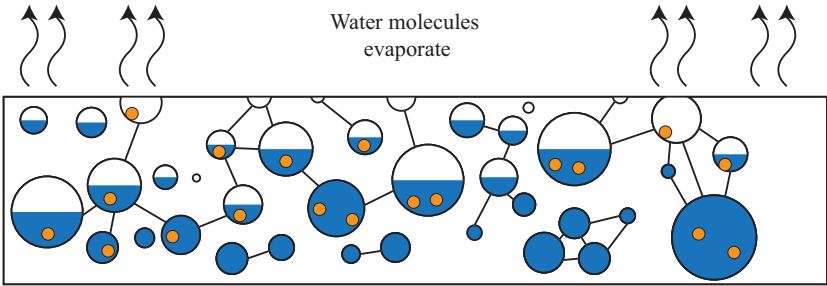Pores are filled with water

Figure A.1: Fresh concrete

Water molecules
evaporate
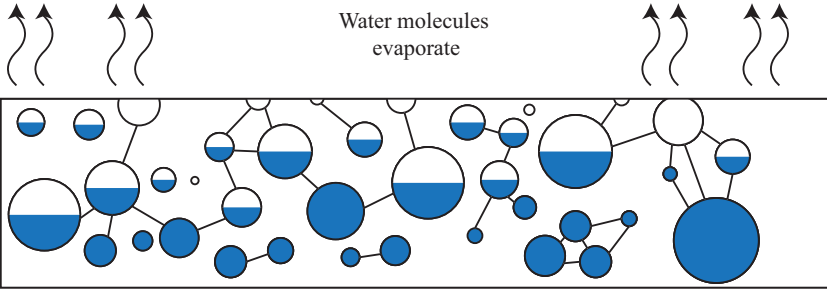
Cement paste hydration consumes water molecules

Figure A.2: Cement paste hydrates and water evaporates

Saline solution
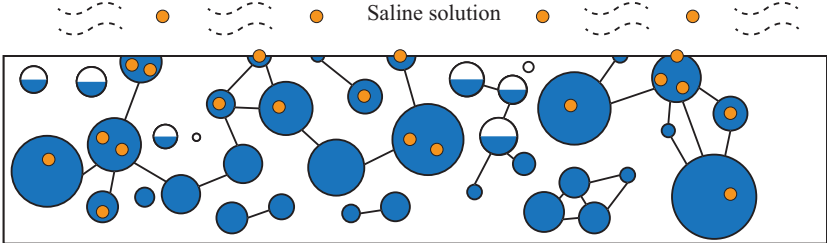
Pores are filled with water and chloride ions

Figure A.3: Chloride contamination

Water molecules
evaporate

Chlorides remain inside concrete and diffuse

Figure A.4: Evaporation after chloride contamination

A IV - Real case study

Motivation

The objective of this study was to locate the presence of chlorides in the deck of the bridge Rödelbachbrucke in Appenzell, Switzerland. The slab forming the deck was built using reinforced concrete. The cover concrete is the concrete located between the asphalt layer and the first rebar layer, it was inspected for chloride contamination, fig. A.1.

Measurement campaign

The campaign was performed within half a day without interrupting traffic. The measurement required the use of off-ground GPR horn antennas and positioning was done using a GPS system. GPR profiles were acquired from the road surface of the bridge deck. The dataset consist of 11 longitudinal parallel profiles, distant of 0.5m, Fig. A.2.

Data processing

The global velocity was determined from the difference in time between the pavement reflection and the slab's bottom reflection, see figure , A.3 and A.4. The thickness of the bridge deck was determined from the construction plan provided in the documentation, A.2. Profiles I, II, IX, X and XI were close to the webs were the thickness of the deck increases. Because of this configuration, these profiles are less precise than the profiles performed in the flat section of the deck. Conductivity was calculated using Time Domain Solution between the pavement reflection and the first rebar layer reflection, however this calculation does not take into account the reflection occurring at the asphalt/concrete interface. This has for consequence that some energy is missing. Conductivity is overestimated in this analysis.
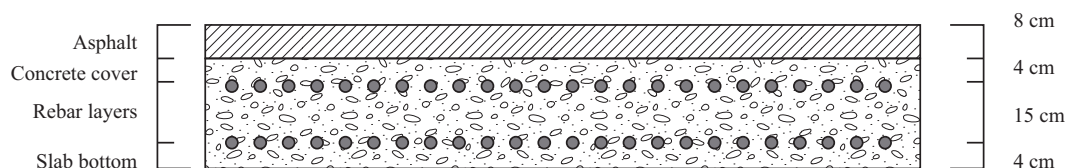

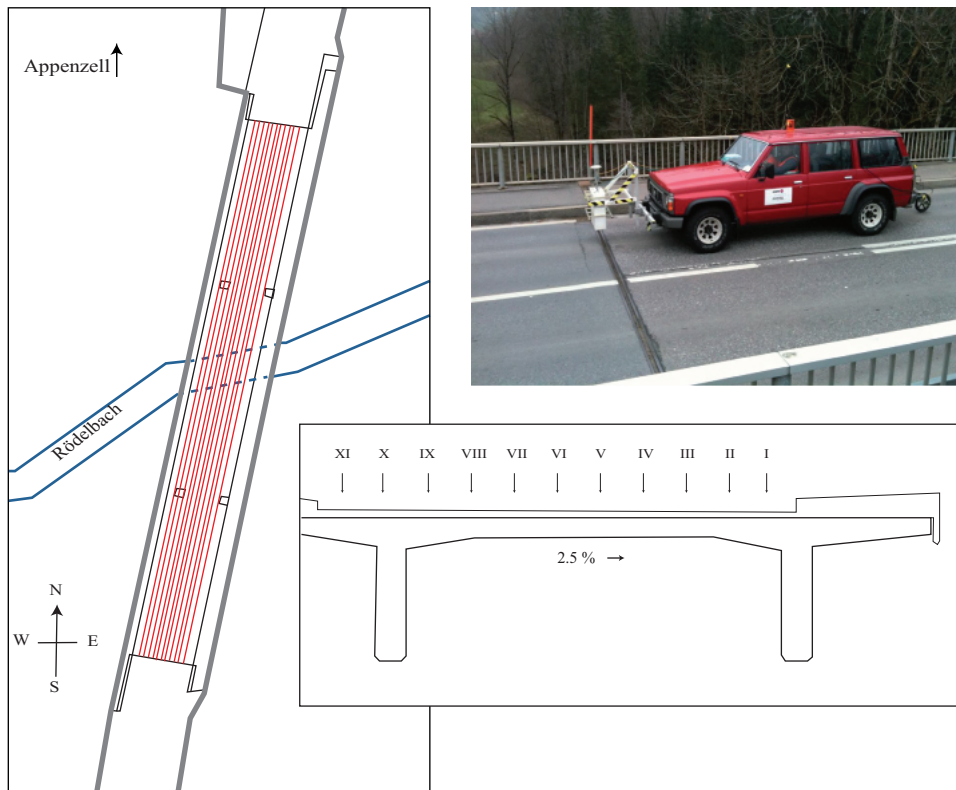Figure A.1: Concrete bridge deck slab
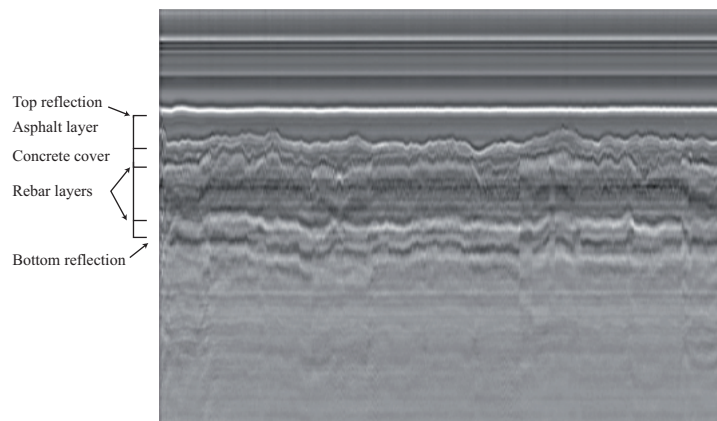
Figure A.2: GPR profiles position and acquisition setup
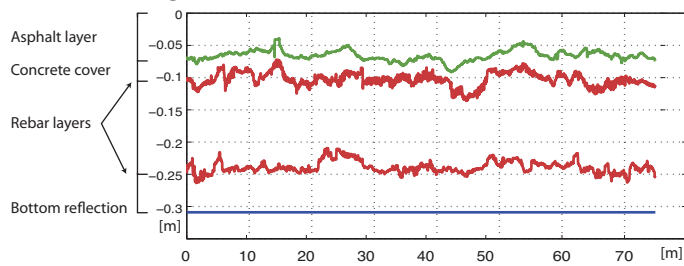

Figure A.3: Reflectors identification

Figure A.4: Thicknesses estimation

Results

The results are presented in 4 maps of the bridge deck slabs , see figure A.5:

The first map depicts the thickness of concrete cover figure A.5(a). The concrete cover was estimated using the global velocity and the time difference between the asphalt/concrete reflection and the first rebar layer, fig.A.4. The profiles recorded on the sides of the bridge have less precision than the ones recorded in the centre of the bridge. The results reveal that the concrete cover is thinner in the centre of the deck. It can also be observed that the concrete cover has thicker zones on the west side of the deck.

The second map depicts the average value of dielectric permittivity for the whole section of the bridge deck, fig.A.5(b). The dielectric permittivity relates the humidity level within concrete, see Chapter 3. As it was calculated for the whole section of the deck, the map depicts the average humidity level of the bridge deck. The results show that the centre of the deck is has an intermediate humidity and the sides of the deck are dry. Few localized areas in the centre of the deck are wet, in red.

The third map depicts the conductivity level of the concrete cover and the asphalt layer fig.A.5(c). The map accounts for the presence of chloride on top of the rebar layer, within asphalt and cover concrete layers. Due to approximations used for calculation, these values are overestimated. The map of chloride distribution reveals that the conductivity is more important in the centre of the bridge deck than on the sides. However, the average chloride level is very low to low, some points have an intermediate quantities of chlorides.

Probing With these results a targeted probing campaign was done on the bridge, the free chloride content of the cores was determined. Compared with GPR results the analysis shows good correspondence.

Conclusions

Ground Penetrating Radar measurements have been conducted on a bridge for condition surveys.The dataset was easily collected using Ground Penetrating Radar 1.2 [GHz] horn-antennas. Data analysis enabled the detection inner geometrical properties of cover concrete, the humidity and the presence of chloride ions of the bridge deck. The cartographic representations of the extent and depth of the damages were produced using GPR results. Three maps to represent chloride contamination, humidity and concrete cover thickness, were provided. GPR results were compared with targeted probing campaign done after the analysis, they showed good correspondence. The information gained from GPR datasets were used for the detailed examination of the structure condition and performance.

Acknowledgment

(a)

(b)

(c)

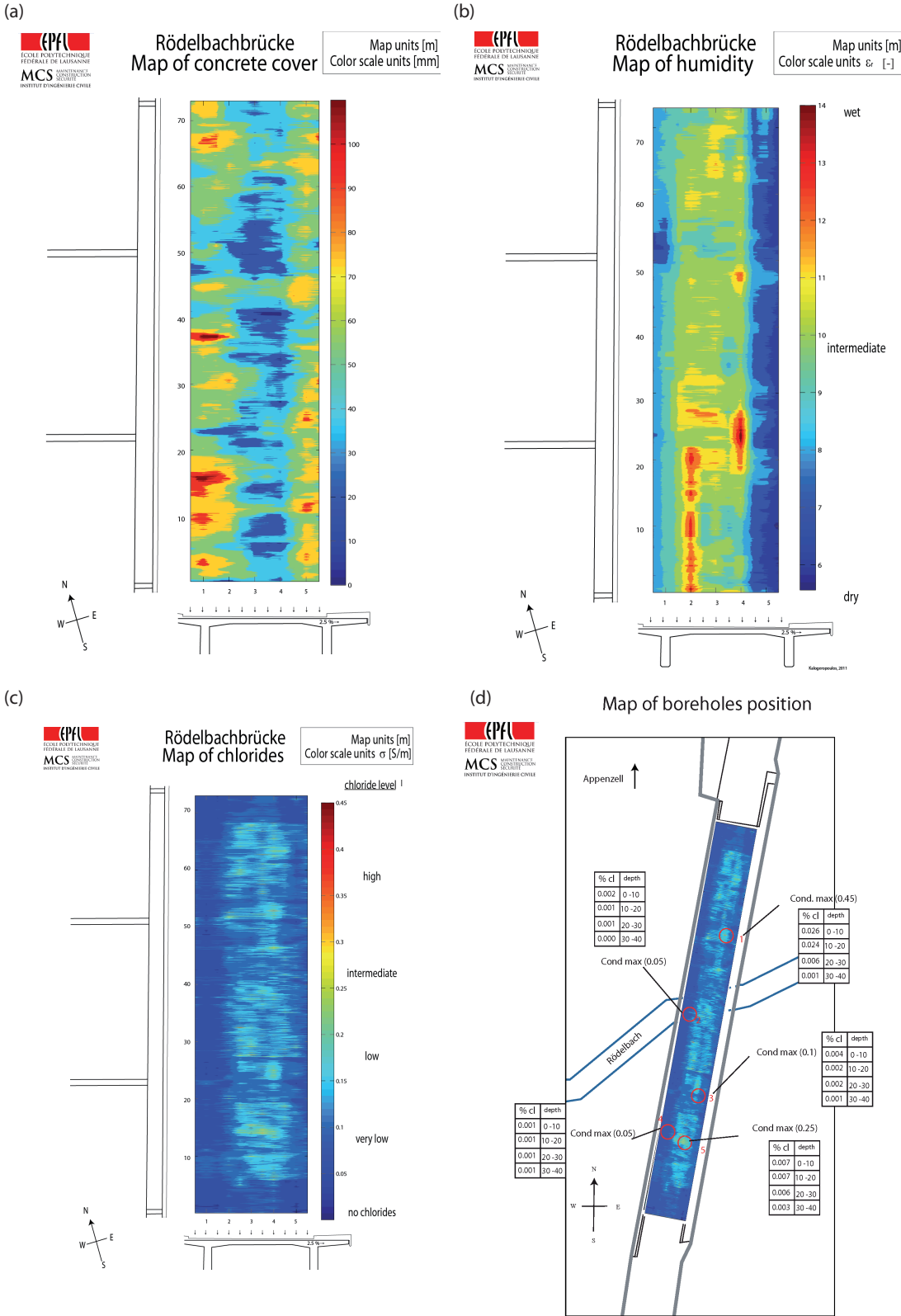(d)

Map of boreholes position

Figure A.5: a) map of concrete cover, b) map of humidity, c) map of chlorides, d) targeted probing results.

Alexis Kalogeropoulos

ENAC IIC MCS
GC B2 402 Bâtiment GC
Station 181015 Lausanne

Tél. +41 21 693 32 93

alexis.kalogeropoulos@epfl.ch
http://people.epfl.ch/alexis.kalogeropoulos

Profile

PhD student

Birth date: 20.03.1978

Nationality: French

Scholarship

2001   Bachelor in Geography, University Paris VII, Paris, France.

2003   Bachelor in Geology, University Paris Sud, Orsay, France.

2004   Master I in Environmental sciences, University of Granada, Spain.

2005   Master II in Applied Geophysics. University Joseph Fourier, Grenoble, France.

2008   2012 Ph.D. student, in Geophysics applied to civil engineering.

Experience

Geophysicist in Geotechnics Karakas & Français SA Lausanne, Switzerland, 2005-2006

Scientist at Road and sealing components lab, EMPA, Dübendorf, Switzerland, 2007-2008

Non-destructive auscultation of patrimonial structures, ANDS, Lausanne, 2009 - today

Scientific contributions

Peer reviewed publications

Chlorides and moisture assessment in concrete by GPR full waveform inversion, Kalogeropoulos,A.; van der Kruk,J.; Hugenschmidt,J.; Busch,S.; Merz,K., Near Surf. Geophys., 2011, 9, 3, 277-285, EAGE

The inspection of retaining walls using GPR, Hugenschmidt,J.; Kalogeropoulos,A., J. Appl. Geophys., 2009, 67, 4, 335-344, Elsevier

Processing strategies for high-resolution GPR concrete inspections, Hugenschmidt,J.; Kalogeropoulos,A.; Soldovieri,F.; Prisco,G., NDT&E Int., 2010, 43, 4, 334-342, Elsevier

Conference proceedings

Processing strategies for high-resolution concrete inspections, Hugenschmidt,J.; Kalogeropoulos,A.; Soldovieri,F.; Prisco,G., Conference proceeding GPR2008, 6 pp, Birmingham, UK

3D GPR inspection of retaining walls, Hugenschmidt,J.; Kalogeropoulos,A.; Mastrangelo,R., Conference proceeding DGG 2008, 78-79, Freiberg, Deutschland

Georadar-Untersuchungen vor, während und nach einer Million Schwerlastüberrollungen auf einer Autobahn, Hugenschmidt,J.; Kalogeropoulos,A., Jahrestagung der Deutschen Geophysikalischen Gesellschaft 2008

GPR full waveform inversion for chlorides and moisture detection in concrete, Kalogeropoulos,A.; Hugenschmidt,J.; van der Kruk,J.; Merz,K., IWAGPR 2009, 190-194, Granada, Spain

Ground Penetrating Radar for condition survey of structures, Kalogeropoulos, A.; Noshiravani, T.; Grandjean, A.; Brühwiler E., Conference SHMII-4 2009 Zürich

Monitoring the evolution of water and chloride in concrete using GPR full-waveform inversion, Kalogeropoulos,A.; van der Kruk,J.; Hugenschmidt,J.;, IWAGPR 2011, Aachen, Germany

Full-waveform inversion of ground penetrating radar data to assess chloride and moisture content in concrete, van der Kruk,J.; Kalogeropoulos,A.; Hugenschmidt,J.; Busch,S.; Merz,K., Conference EGU2011, Geophys. Res. Abstr., 2011, 13, EGU2011-6878 (1 p.), EGU; Copernicus, Vienna, Austria

Hi-resolution 3d condition survey of a masonry arch bridge using Ground Penetrating radar dataset, Kalogeropoulos,A.; Brühwiler E., Conference SMAR2011 Dubaï.

Reports

Pilotstudie zur Evaluation einer mobilen Grossversuchsanlage für beschleunigte Verkehrslastsimulation auf Strassenbeläge, Arraigada, M., Kalogeropoulos, A., Hugenschmidt, J., Partl, M.N., Caprez, M., Rabaiotti, C., Eidgenössisches Departement für Umwelt, Verkehr, Energie und Kommunikation, Bundesamt für Strassen. ASTRA 2004/018, Report Nr 1261, (2009)

.